Clumped-Isotope Thermometry of Magnesium Carbonates in Ultramafic Rocks

Pablo García del Real[1*], Kate Maher[1], Tobias Kluge[2,3], Dennis K. Bird[1], Gordon E. Brown, Jr[1,4], Cédric M. John[2]

[1]*Department of Geological Sciences, School of Earth, Energy, and Environmental Sciences, Stanford University, Stanford, CA 94305-2115, USA.*
[2]*Department of Earth Science and Engineering and Qatar Carbonate and Carbon Storage Research Centre (QCCSRC), Imperial College London, Prince Consort Road, London SW7 2AZ, UK*
[3]*Institute of Environmental Physics, Universität Heidelberg, Germany*
[4]*Department of Photon Science and Stanford Synchrotron Radiation Lightsource, SLAC National Accelerator Laboratory, Menlo Park, CA 94025, USA*

**corresponding author: e-mail gdelreal@stanford.edu; phone +1 (650) 515 1864; fax +1 (650) 725-2199*

Abstract

Magnesium carbonate minerals produced by reaction of H_2O-CO_2 with ultramafic rocks occur in a wide range of paragenetic and tectonic settings and can thus provide insights into a variety of geologic processes, including (*1*) deposition of ore-grade, massive-vein cryptocrystalline magnesite; (*2*) formation of hydrous magnesium carbonates in weathering environments; and (*3*) metamorphic carbonate alteration of ultramafic rocks. However, the application of traditional geochemical and isotopic methods to infer temperatures of mineralization, the nature of mineralizing fluids, and the mechanisms controlling the transformation of dissolved CO_2 into magnesium carbonates in these settings is difficult because the fluids are usually not preserved. Clumped-isotope compositions of magnesium carbonates provide a means to determine primary mineralization or (re)equilibration temperature, which permits the reconstruction of geologic processes that govern magnesium carbonate formation. We first provide an evaluation of the acid fractionation correction for magnesium carbonates using synthetic magnesite and hydromagnesite, along with natural metamorphic magnesite and low-temperature hydromagnesite precipitated within a mine adit. We show that the acid fractionation correction for magnesium carbonates is virtually indistinguishable from other carbonate acid fractionation corrections given current mass spectrometer resolution and error. In addition, we employ carbonate clumped-isotope thermometry on natural magnesium carbonates from various geologic environments and tectonic settings. Cryptocrystalline magnesite vein deposits from California (Red Mountain magnesite mine), Austria (Kraubath locality), Turkey (Tutluca mine, Eskişehir district) and Iran (Derakht-Senjed deposit) exhibit broadly uniform Δ_{47} compositions that yield apparent clumped-isotope temperatures that average 23.7 ± 5.0°C. Based on oxygen isotope thermometry, these clumped-isotope temperatures suggest mineralization at shallow crustal depths in the presence of meteoric water. Hydrous magnesium carbonates from a 400-km latitudinal transect along the serpentinized-peridotite bodies of the California Coast Ranges record clumped-isotope temperatures between 14.2 and 22.7 ± 2.8°C, in agreement with historical maximum temperatures during the rainy season for California. Talc-carbonate alteration of ultramafic rocks in Greenland (Isua Supracrustal Belt) and Vermont (Ludlow) yields clumped-isotope alteration temperatures of magnesite and dolomite between 326 and 490°C, broadly consistent with paragenesis and thermodynamic analysis for CO_2 metasomatism of ultramafic rocks. These metamorphic carbonates extend the applicability of clumped-isotope thermometry to high-temperature magnesium carbonate systems and indicate equilibrium blocking temperatures for magnesite of ~ 490°C. Our study demonstrates the applicability of the clumped isotope approach to provide information on the formation of magnesium carbonates as ore resources, surface records of climate, and metamorphic assemblages.

Keywords**:** magnesite, hydrous magnesium carbonates, clumped-isotope thermometry, carbon capture and storage.

1. Introduction

Magnesite ($MgCO_3$) and hydrated magnesium carbonates form in a wide variety of geologic environments and are ubiquitous throughout the geologic record. Considered to be a potentially major reservoir of carbon in the Earth's mantle (Wang *et al*., 1996; Isshiki *et al*., 2004; Hazen and Schiffries, 2013), magnesite is stable at pressures and temperatures that encompass metamorphic and hydrothermal systems, continental and oceanic sedimentary environments, and shallow crustal and surface processes (Bristol, 1972; McGetchin and Besancon, 1973; Lappin and Smith, 1978; Pohl, 1990; Zhang and Liou, 1994; Sherlock and Logan, 1995; Melezhik *et al*., 2001; Schroll, 2002; Hansen *et al*., 2005; Boschi *et al*., 2009; Falk and Kelemen, 2015). In contrast, hydrous magnesium carbonates are restricted to Earth's surface and occur in the form of lacustrine deposits, incrustations and stalactites in cave systems and mine adits, and as weathering products in ultramafic mine tailings, soil profiles and road cuts (Genth and Penfield, 1890; Wise and Moller, 1995; Braithwaite and Zedef, 1996; Cañaveras *et al*., 1999; Zedef *et al*., 2000; Power *et al*., 2009; Wilson *et al*., 2009; Wilson *et al*., 2010; Pronost *et al*., 2012; Beinlich and Austrheim, 2012; Harrison *et al*., 2013; Power *et al*., 2014; Wilson *et al*., 2014).

Magnesium carbonates hosted in ultramafic rocks represent a geologically stable, long-term repository for CO_2 at crustal conditions and their formation parameters can provide geologic constraints for engineered CO_2 capture and storage (CCS) (Kelemen, 2008; Matter and Kelemen, 2009; Kelemen et al., 2011; Power *et al*., 2013a; Power *et al*., 2013b). Field observations, structural relationships, and classical stable isotope thermometry of ultramafic-hosted cryptocrystalline magnesite have been applied to various extents (Petrov, 1980; Pohl, 1990; Jedrysek and Halas, 1990; Fallick *et al*., 1991; Abu-Jaber and Kimberley, 1992; Zedef *et al*., 2000; Ghoneim *et al*., 2003; Gartzos, 2004; Ece et al., 2005; Mirnejad *et al*., 2008; Jurković *et al*., 2012; Streit *et al*., 2012; Oskierski *et al*., 2013; Quesnel *et al*., 2013; Kahya and Kuşcu, 2014; Ulrich *et al*., 2014), with relatively limited focus on hydrous magnesium carbonates (Power *et al*., 2014). However, the temperatures of formation and the origin and composition of mineralizing solutions associated with natural magnesium carbonate precipitation remain poorly constrained, although both are critical to determining the genetic model for the many large-scale deposits.

The presence of cryptocrystalline magnesite deposits and hydrous magnesium carbonates in obducted segments of serpentinized peridotite and serpentinite suggests that carbonate mineralization postdates serpentinization and, by inference, occurs at temperatures at or lower than serpentinization temperatures (50-300°C; Evans, 2010). Coupled stable isotope compositions ($\delta^{13}C$ and $\delta^{18}O$) of ultramafic-hosted magnesium carbonates have been essential in approximating the temperature of mineralization, the types of mineralizing fluids, and sources of CO_2. However, the oxygen isotope composition of magnesite ($\delta^{18}O_{mgs}$) cannot be used to independently establish the temperature of crystallization, T_{mgs}, or to calculate the oxygen isotope composition of the mineralizing solution ($\delta^{18}O_{fluid}$) in equilibrium with the carbonate mineral. In this case, either T_{mgs} or $\delta^{18}O_{fluid}$ need to be assumed to satisfy the oxygen isotope fractionation between magnesite ($\delta^{18}O_{mgs}$) and the fluid ($\delta^{18}O_{fluid}$), as given by the equation

$$\delta^{18}O_{mgs} - \delta^{18}O_{fluid} = (A \times 10^6)/T_{mgs}^2 + B \quad (1)$$

where *A* and *B* are determined experimentally (Faure and Mensing, 2005). However, there are no experimental data specific for magnesite. Although both T_{mgs} and $\delta^{18}O_{fluid}$ can be resolved using other approaches (*e.g.*, fluid inclusions, thermodynamic stability calculations, or field observations), we apply a different approach using carbonate clumped-isotope thermometry, which independently defines T_{mgs} without *a priori* knowledge of the isotopic composition of the mineralizing solution (Eiler, 2007). This approach has been shown to yield accurate temperatures of formation for a wide range of geologic environments and synthetic carbonates. For a detailed review on the applicability of carbonate clumped isotope geochemistry, the reader is referred to recent reviews by Eiler *et al.* (2014) and Huntington and Lechler (2015).

We first evaluate the fractionation correction required for acid decomposition of magnesium carbonates in anhydrous phosphoric acid to release CO_2 for analysis (*e.g.*, McCrea, 1950). For the acid fractionation evaluation, we use synthetic magnesite and hydromagnesite, along with metamorphic magnesite and low-temperature hydromagnesite precipitated within a mine adit. These measurements are complemented by additional magnesite samples (Streit *et al*., 2012; Falk and Kelemen, 2015). We also determine clumped-isotope temperatures of formation of: (*1*) cryptocrystalline magnesite from California (USA), Austria, Turkey and Iran, (*2*) nesquehonite ($MgCO_3 \cdot 3H_2O$), hydromagnesite ($Mg_5(CO_3)_4(OH)_2 \cdot 4H_2O$), dypingite ($Mg_5(CO_3)_4(OH)_2 \cdot 5H_2O$) and artinite ($Mg_2(CO_3)(OH)_2 \cdot 3H_2O$) from surface deposits in the peridotite-serpentinite belt of the California Coast Ranges; and (*3*) high-temperature magnesite and dolomite related to talc-carbonate alteration of Archean crust (Isua, Greenland) and serpentinite interspersed in the Moretown Formation (Vermont, USA). High-temperature carbonates provide additional calibration constraints and empirical insights into apparent equilibrium blocking temperatures, and extend the use of clumped-isotope thermometry of magnesium carbonates to high-temperature environments. Clumped-isotope temperatures provide new insights into mineral paragenesis and fluid sources related to the alteration of ultramafic rocks on the surface and at crustal depths, with particular emphasis on the California deposits.

2. Geologic Setting and Paragenesis

Samples described below are summarized in Table 1 according to sample name, mineralogy, location, and the expected or independently constrained temperature of mineralization. Locations of the samples are shown in Fig. 1a and detailed locations for California samples are shown in Fig. 1b. Additional descriptions of the samples are provided in Appendices A and B, including X-ray diffraction (XRD) patterns confirming mineralogy and dominant phases (Fig. A1), and end-member crystal structures of magnesite (Fig. A2) and hydrous magnesium carbonates (Fig. A3).

2.1 Cryptocrystalline magnesite

Cryptocrystalline magnesite (also referred to in the literature as *Kraubath*-type, *bone magnesite*, or *gel magnesite*) hosted in ultramafic rocks is an aggregate of euhedral magnesite crystal clusters (~3 μm) and individual, fine (<1 μm) euhedral magnesite crystals held within a matrix of smaller (<0.1 μm) spherical aggregates of crystalline magnesite (Figs. 2a-2b). Cryptocrystalline magnesite, which is generally bright white and has conchoidal fracture, is devoid of fluid inclusions and does not exhibit pseudomorphic replacement textures from the host ultramafic rock (Fig. 2c). Ore-grade cryptocrystalline magnesite samples were obtained from the Red Mountain Magnesite Mine in the peridotite segment of the Del Puerto Ophiolite (DPO) of the California Coast Ranges (Fig 1b; Table 1). The magnesite samples are representative of the various modes of cryptocrystalline magnesite from different sections and depths of the Red Mountain vein system, namely massive magnesite veins (10's of meters in width and >100's of meters in length and depth; Fig. 3a; samples *SD10-2*, *DV10-27C* and *DV10-6*), veinlets (~10 cm wide; Fig. 3b; sample *DV10-21B*), nodules (~30 cm diameter average; Fig 3c; samples *DV10-21A* and *N6V10-2A*), and brecciated purple magnesite (sample *RM09-12II*). The cryptocrystalline magnesite samples from the Red Mountain mine are complemented by samples from other regions (Fig. 1a): (*1*) the type locality for cryptocrystalline magnesite in Austria (Kraubath deposit; sample *AU-15*) (Redlich, 1909; Pohl, 1990; Horkel *et al*., 2009); (*2*) Turkey (Tutluca open pit magnesite mine, Eskişehir province, Turkey; sample *070815-7*; Kahya and Kuşcu, 2014); and (*3*) Iran (Derakht-Senjed magnesite deposit; sample *dhs23*) hosted in serpentinized peridotite. Temperatures of formation of cryptocrystalline magnesite in various deposits worldwide vary from ~10 to 100°C, based on oxygen isotope thermometry and assuming $\delta^{18}O_{fluid}$ compositions of mineralizing waters specific to each locality (references and data in Table A1).

2.2 Hydrous (and hydroxyl) magnesium carbonates

Hydrous magnesium carbonates were collected from surface exposures of several ultramafic bodies distributed in a 400-km latitudinal expanse along the California Coast Ranges (Fig. 1b and Table 1). From north to south: (*1*) hydromagnesite nodules from serpentinite at the McLaughlin Reserve (Figs. 4a-4b; sample *MCL-2*); (*2*) hydromagnesite nodules from road cuts traversing the Del Puerto peridotite (Fig. 4c-4d; sample *RC1*); (*3*) hydromagnesite nodules from the New Idria serpentinite, San Benito County, California (Fig. 4e; sample *09-NI-3*), and (*4*) artinite crystals from a different area of the New Idria serpentinite (Fig. 4f; sample *10-NI-1*). Detailed description of each locality is provided in Appendix B.

Historical climate data are employed to constrain the possible precipitation and temperature conditions that trigger the formation of surface hydrous magnesium carbonates in California. Figures A4 and A5 show a compilation of precipitation and temperature data from several weather stations that cover a similar latitudinal expanse and are in close proximity to the sampling location of hydrous magnesium carbonates (Fig. 1b; Table A3 and Appendix B). The corresponding formation period for surface magnesium carbonates in California likely occurs when rains have provided water to the exposed ultramafic rocks and evaporative concentration drives supersaturation with respect to the hydrous magnesium phases. We thus infer that surface magnesium

carbonate formation is expected to happen during the rainy winter months from October to April at maximum average temperature ~15 to 25°C (Figs. A4 and A5).

2.3 Red Mountain mine adit hydrous magnesium carbonates

Mine adit samples consist of fine to cryptocrystalline white and transparent magnesium carbonates that coat the walls and ceilings of various sections of the Red Mountain mine adits (Fig. 5a). Two apparent cogenetic phases can be distinguished morphologically: a crustiform-type coating of admixed hydromagnesite and minor dypingite (Figs. 2d-2f, 5b-5d; sample *DPT12-10 crust*) that covers the exposed host rock and has shiny, pearl-like appearance (Figs. 5b-5c); and powdery, salt-like, transluscent nesquehonite that develops on the crustiform-type coating (Figs. 5b-5c; sample *DPT12-10 salt*). Both samples were collected 208.6 m from the portal entrance of the mine where the temperature appears to be constant at 11.3°C, based on repeated temperature measurements throughout the mine system (refer to figure caption of Fig. 5a for details). We use the hydromagnesite sample (*DPT12-10 crust*) as a low-temperature calibration point for the acid correction fractionation as discussed in Section 4.1. Additional description of mine adit samples is provided in Appendix B.

2.4 High-temperature carbonates

2.4.1 Magnesite and Dolomite (Isua, Greenland)

Cogenetic magnesite and dolomite occur in carbonate-talc veins within serpentinized dunite-peridotite of the Eoarchean Isua supracrustal belt, Greenland (Fig. 1a; Nutman *et al*., 1984; Rose *et al*., 1996; Pope *et al*., 2012; Szilas *et al*., 2015). The sampled vein is ~30 cm in width and is exposed for several meters in outcrop (Fig. 6a). Both dolomite (sample *14-05 White*) and magnesite (sample *14-05 Red*) occur intimately intergrown with talc (Fig 6b). The carbonates represent the metamorphic mineral assemblage talc + antigorite ± olivine ± dolomite ± magnesite, which independently constrains the temperature of alteration between 430-490°C over the range of likely pressure conditions (0.5 to 5 kb) and CO_2 compositions (Trommsdorff and Evans, 1977; Dymek *et al.*, 1988; Bucher and Grapes, 2011). We adopt a temperature of 450°C as representative of the invariant point defined by the assemblage and for consistency with retrograde metamorphic conditions at ~450°C estimated for the petrogenesis of Isua rocks as reported by Dymek *et al.*, 1988. We use a temperature of 450°C for the high-temperature magnesite acid fractionation point (sample *14-05 Red*; Section 4.1). Supplementary description of the samples is given in Appendix B.

2.4.2 Dolomite (Ludlow, Vermont, USA)

Dolomite from the Argonaut Talc Mine (formerly Luzenac), Ludlow, Vermont (Figs. 1a and 6c; sample *08SVT-4A*) is related to hydrothermal talc-carbonate alteration of serpentinite that is part of the ultramafic belt in western New England (Sanford, 1982; Robinson *et al*., 2006). Based on the descriptions of Robinson *et al*. (2006), the alteration is characterized by talc and magnesite, and when dolomite is present, chlorite also occurs.

Thus the assemblage talc+magnesite+dolomite+chlorite is in contact with siliceous metamorphic rocks that supply the additional Ca and Al necessary for dolomite and chlorite mineralization, respectively. Possible temperatures of carbonate mineralization at Ludlow, Vermont are given by peak metamorphic conditions in neighboring units (535-635°C; Vance and Holland, 1993; Armstrong and Tracy, 2000), assumed temperatures of talc-carbonate alteration in western New England (450-530°C; Sanford, 1982), and magnesite-talc alteration equilibrium (430-490°C; Bucher and Grapes, 2011). Ancillary information of sample *08SVT-4A* is given in Appendix B.

2.5 Synthetic magnesite from olivine dissolution

Magnesite was produced from olivine (Forsterite, Fo_{92}) dissolution experiments at 60°C, 100 bars pCO_2, 0.5M NaCl, and variable water-rock ratios (20:1 and 50:1) (Johnson *et al.*, 2014; samples *0209* and *1210P*). Magnesite displays spiral growth producing nodules that reach diameters of ~15 μm (Fig. 7a) and precipitates at minimum average rates of 1.40×10^{-13} mol cm^{-2} s^{-1}. Concomitant to magnesite precipitation, amorphous silica also formed as large sheets and as coatings on the olivine grains (Fig. 7a). The reader is referred to Johnson *et al.* (2014) for additional information on the mineralogy, carbon content, surface chemical composition, bulk chemistry of the samples, as well as a comprehensive discussion of the experimental apparatus used for olivine dissolution and magnesite precipitation. Both of the samples (*0209* and *1210P*) were employed in the acid-correction of magnesium carbonates (Section 4.1).

2.6 Synthetic hydromagnesite

Hydromagnesite (samples *Mg-1* and *Mg-3*) was synthesized at 79.9 ± 0.5°C following the precipitation methods reported in Kluge and John (2015), which are similar to the methods of Kim and O'Neil (1997) used for calcite. Briefly, 500 mL of de-ionized water (18 MΩ cm) were super-saturated with respect to $CaCO_3$ by dissolving ~360 g of high-purity calcite. Addition of $MgCl_2(H_2O)_6$ at moderate concentrations (0.2-0.7 mol/L) triggered the formation of hydromagnesite (Fig. 7b). Mineral formation was induced by controlled purging of the solution with N_2 at ~1 bubble per second. The precipitates were filtered and air-dried. XRD analyses (Fig. A1d) confirmed that the precipitates were hydromagnesite (88%) and aragonite (12%) for sample *Mg-1* and ~100% for sample *Mg-3* (Fig. 7b; Kluge and John, 2015). Samples *Mg-1* and *Mg-3* were used in the acid fractionation evaluation presented in Section 4.1.

3. Methods

3.1 Carbonate clumped-isotope thermometry

Carbonate clumped-isotope thermometry is based on the thermodynamic ordering of carbon and oxygen isotopes in the carbonate species dissolved in the mineralizing fluid and preserved in the crystal structure of carbonate minerals. Although the majority of applications of clumped-isotope thermometry have focused on calcite (*e.g.*, Bristow *et al.*, 2011; Daëron *et al.*, 2011; Suarez *et al.*, 2011; Swanson *et al.*, 2012; Streit *et al.*,

2012; Loyd *et al.*, 2012; Henkes *et al.*, 2014; Wacker *et al.*, 2014; Kluge *et al.*, 2015; Kluge and John, 2015), aragonite (*e.g.*, Defliese *et al.*, 2015), dolomite (*e.g.*, Ferry *et al.*, 2011; Swanson *et al.*, 2012; Streit *et al.*, 2012; Loyd *et al.*, 2012; Sena *et al.*, 2014; Vandeginste *et al.*, 2014; Dale *et al.*, 2014), and siderite (Fernandez *et al.*, 2014), magnesite and hydromagnesite have been also studied (Streit *et al.*, 2012; Falk and Kelemen, 2015; Quesnel *et al.*, 2016). The distribution of clumped carbonate isotopologues is defined here by the reaction in terms of magnesite, $MgCO_3$ (Fig. A2a):

$$Mg^{13}C^{16}O_3 + Mg^{12}C^{18}O^{16}O_2 \Leftrightarrow Mg^{13}C^{18}O^{16}O_2 + Mg^{12}C^{16}O_3 \quad (2)$$

where the magnesite isotopologue $Mg^{12}C^{16}O_3$ represents the most abundant isotopic configuration containing the carbonate isotopologue CO_3^{2-} with a mass of 60 amu (Fig. A2b). In contrast, the magnesite isotopologue $Mg^{13}C^{18}O^{16}O_2$ denotes bonding between the two heavy isotopes of carbon (^{13}C) and oxygen (^{18}O). This second carbonate isotopologue of mass 63 is increasingly favored in the magnesite structure with decreasing temperature (Fig. A2c). Multiply substituted isotopologues are comprised of two or more rare isotopes and their abundance is governed by thermodynamic parameters that depend on the rotational and vibrational frequencies of the relevant bonds (Wang *et al.*, 2004). The abundance of the ^{13}C-^{18}O bonds contained in the $Mg^{13}C^{18}O^{16}O_2$ configuration is measurable in CO_2 evolved from magnesite via reaction with phosphoric acid (Fig. A2c), and is proportional to the CO_2 isotopologue of mass 47 (*i.e.* $^{47}CO_2$, ^{13}C-^{18}O-^{16}O) (Ghosh *et al.*, 2006). The abundance of the $^{63}CO_3^{2-}$ isotopologue in the magnesite crystal structure, and by definition the evolved $^{47}CO_2$, is independent of the bulk $\delta^{18}O_{fluid}$ and $\delta^{13}C_{fluid}$ composition of the parent fluid from which the magnesite (or a hydrous magnesium carbonate) formed, rendering it a proxy for temperature of mineralization.

The total abundance of $^{47}CO_2$ in a given sample is evaluated with regard to its stochastic distribution at high temperatures (>1000°C) and reported using the Δ_{47} notation (Eiler and Schauble, 2004; Wang *et al.*, 2004), such that

$$\Delta_{47} = \left[\frac{R^{47}}{2R^{13}\cdot R^{18} + 2R^{17}\cdot R^{18} + R^{13}\cdot (R^{17})^2} - \frac{R^{46}}{2R^{18} + 2R^{13}\cdot R^{17} + (R^{17})^2} - \frac{R^{45}}{R^{13} + 2R^{17}} + 1 \right] \quad (3)$$

where Δ_{47} (reported as per mil, ‰) is calculated from measurements of masses 44 through 47, and is represented as ratios with respect to mass 44 (*e.g.*, R^{47} is $^{47}CO_2/^{44}CO_2$). R^{13} ($^{13}C/^{12}C$) and R^{18} ($^{18}O/^{16}O$) are derived from measured $\delta^{13}C$ and $\delta^{18}O$ values. R^{17}($^{17}O/^{16}O$) is derived from R^{18} assuming mass-dependent fractionation (Affek and Eiler, 2006). The Δ_{47} values of magnesium carbonates are a function of temperature and decrease with increasing temperature (Schauble et al., 2006; Guo et al., 2009). Depending on the mineralogy and the rate of cooling, the preserved Δ_{47} compositions may record "apparent equilibrium blocking temperatures," indicating that the isotope-exchange reaction defined by Equation 2 does not proceed in any direction (Stolper and Eiler, 2015).

To determine the temperature of magnesium carbonate mineralization, we evaluate the experimental calcite clumped-isotope calibration of Kluge *et al.* (2015):

$$\Delta_{47} = 0.98\cdot(-3.407\cdot10^{9}/T^{4}+2.365\cdot10^{7}/T^{3}-2.607\cdot10^{3}/T^{2}-5.880/T+0.293) \quad (4)$$

where *T* is temperature in degrees *K*. The temperature dependence of Equation 4 follows the theoretical prediction of Schauble *et al.* (2006), which coincides with independent studies that observed an agreement between the experimental and theoretical temperature curve for a variety of carbonate minerals from biogenic and inorganic origin (Henkes *et al*., 2013; Fernandez *et al*., 2014; Wacker *et al*., 2014; Petrizzo *et al*., 2014; Defliese *et al*., 2015), including magnesite. "We have chosen the Kluge et al. (2015) line (Equation 4) as temperature calibration for carbonate Δ_{47} values because it covers a wide range of temperatures (wider than any other calibrations), and was established in the same laboratory using the same CO_2 extraction, purification and mass spectrometric measurement techniques and corrections applied to the magnesium carbonates of this study. Therefore, any issues related to interlaboratory differences in sampling processing and data evaluation can be avoided."

3.2 Sample treatment of carbonates for clumped-isotope analysis

Samples were ground depending on hardness using an agate mortar or a handheld diamond-head drill. Powdered samples were sieved to yield grain sizes between 50 and 125 μm in diameter. Samples of 5-8 mg were separated from the sieved powder for acid digestion. Synthetic olivine-magnesite samples consisted of ~140 mg of material due to variable magnesite content as some of the mass was contributed by olivine. Thus a larger mass was needed to ensure sufficient CO_2 yield. Samples were inserted into the inlet part of a reaction vessel that allowed sample storage separate from the anhydrous 105% phosphoric acid (for details regarding the reaction vessel refer to Kluge and John, 2015). Approximately 1.5 to 3 mL of phosphoric acid were used per sample. The reaction vessel, containing carbonate sample and phosphoric acid, was evacuated prior to digestion for 30 minutes and reached pressures of 10^{-1} to 10^{-2} mbar before starting the acid digestion. All samples were digested for 1 h in a continuously stirred reaction vessel at 90 ± 1°C. We note that cryptocrystalline magnesite reaches an average yield of 75±7% after 1 hour, with 100% digestion being achieved after 2 hours. Whereas a limited influence of the digestion yield is obvious for $\delta^{13}C$ values, no significant variations were observed for $\delta^{18}O$ and Δ_{47} values after 40 min (<0.2 ‰ and <0.02 ‰, respectively; Test of acid digestion yield and related isotopic variations in Appendix B). The effect of lower yields (~80%) at 90°C and 1 hr is thus negligible for clumped-isotope measurements, which are undistinguishable from magnesium carbonates digested for longer periods of time. Evolved CO_2 was continuously collected in a liquid-N_2 cooled trap and cleaned using a procedure analogous to that of Dennis and Schrag (2010) and described in detail for the Imperial College laboratory in Dale *et al*., (2014). First, non-condensable gases were cryo-distilled from the liquid N_2-cooled trap. Subsequently, water was separated from the gas by switching to a dry-ice ethanol cooled glass trap that retains water and releases the CO_2. The dry CO_2 gas was then passively passed through a glass trap filled with silver wool and another trap densely packed with Porapak Q (filled length: 13 cm, inner diameter: ~8 mm) held at −35°C. Finally, the purified CO_2 gas was transferred to the mass spectrometer for analysis.

3.3 Mass spectrometric analysis and data evaluation

Carbonate samples were analyzed for clumped-isotope compositions in the Qatar Stable Isotope Laboratory at Imperial College London, UK. Mass spectrometric analyses were performed with two Thermo MAT 253 following analytical procedures described by Dale *et al.* (2014). A measurement consists of 8 acquisitions with 7 cycles per acquisition. Each cycle included a peak center, background measurements and an automatic bellow pressure adjustment aimed at a 15V signal at mass 44. The sample gas was measured against an Oztech standard ($\delta^{13}C_{VPDB}$ = −3.63 ‰, $\delta^{18}O_{VPDB}$ = −15.79 ‰; and $\delta^{13}C_{VPDB}$ = −3.62 ‰, $\delta^{18}O_{VPDB}$ = −15.73 ‰, respectively). Heated gases (1000°C), water-equilibrated gases (25°C, 50°C, 80°C) and two carbonate standards (Carrara Marble, ETH3) were measured regularly and used for conversion to the carbon dioxide equilibrium scale (CDES) of Dennis *et al*. (2011). Raw data (Δ_{47} values) were linearity corrected using heated gas data, following the approach of Huntington et al. (2009). Water-equilibrated and heated CO_2 gases established an absolute reference frame as proposed by Dennis *et al*. (2011). The values of Carrara Marble and ETH3 standards were determined based on this equilibrated gas scale (0.312 and 0.634 ‰, respectively). Adding the acid-fractionation correction used in Dennis *et al.* (2011) and Meckler et al. (2014) leads to or close to the accepted values (0.385-0.403 ‰ for Carrara Marble and 0.705 % for ETH3 - "Iso C" in Meckler *et al*. 2014). Small differences may be due to the statistical nature of the data and because we independently determined the value of these carbonate standards. The correction for acid fractionation was added to the sample values after transfer of the linearity corrected value into the absolute reference frame. Contamination was monitored using signals from masses 48 and 49 and measurements were rejected based on elevated 48 and 49 signals (Kluge *et al*., 2015).

Carbonate $\delta^{18}O_{VPDB}$ and $\delta^{13}C_{VPDB}$ values were determined concurrently with the clumped-isotope measurements. Oxygen isotope ratios were calculated using the acid fractionation factors of Das Sharma *et al.* (2002) for magnesite and hydromagnesite (assumed to be similar to magnesite) and Rosenbaum and Sheppard (1986) for dolomite. Mixtures of carbonate minerals (sample *Mg-1*) were evaluated using the corresponding fractionation factors for aragonite (Kim and O'Neil, 1997) and the relative ratio of the carbonate fractions.

The analytical uncertainties of Δ_{47}, $\delta^{18}O$ and $\delta^{13}C$ measurements were calculated by Gaussian error propagation. We used the standard error (SE) of the mean in the case of replicate analyses and the standard deviation for a single measurement (1σ: ±0.02 ‰ for Δ_{47}, ±0.2 ‰ for $\delta^{18}O$, and ±0.1 ‰ for $\delta^{13}C$). The typical standard deviation of a single measurement was deduced from the long-term analysis of carbonate standards and agrees with the sample reproducibility.

4. Results

Natural (n=19) and synthetic (n=4) magnesite and hydrous magnesium carbonate samples were analysed at least twice and up to six times, except for two samples (Table 2). Average measured Δ_{47} values, acid fractionation correction, acid fractionation-corrected Δ_{47} values, and $\delta^{18}O_{VSMOW}$ and $\delta^{13}C_{VPDB}$ compositions are summarized in Table 2. Measurement data (reference gases, standards, and samples) are provided as an

electronic annex file. To determine the acid-correction applicable to magnesium carbonates, we evaluate the calcite Δ_{47}-T relationship of Kluge *et al*. (2015) against the synthetic samples and natural samples with known temperatures of formation (Section 4.1). Details on the computations of corresponding O ($\delta^{18}O_{fluid}$) and C ($\delta^{13}C_{CO2}$) isotopes of the mineralizing fluid are included in Sections 4.4 and 4.5, respectively.

4.1 Δ_{47} acid reaction correction for magnesite and hydrous magnesium carbonates

Carbon dioxide gas ($CO_{2(g)}$) produced from phosphoric acid digestion of mineral carbonates was analyzed mass-spectrometrically to determine the clumped-isotope value (Δ_{47}) of each sample. The conversion of solid carbonate into $CO_{2(g)}$ via acid digestion involves a fractionation for Δ_{47} (*i.e.* $\alpha_{CO2(g)-\Delta47}$) that is dependent on the acid digestion temperature (T_{acid}) and could be theoretically and experimentally different depending on the type of carbonate mineral (Guo *et al.*, 2009; Murray *et al.*, 2016). However, experimental and empirical data show that the effect of mineralogy during acid digestion is negligible for $CaCO_3$ polymorphs (Wacker *et al.*, 2014; Defliese *et al*., 2015; Kluge *et al*., 2015; Kluge and John, 2015), siderite (Fernandez *et al*., 2014) and carbonate-bearing bioapatite (Eagle *et al*., 2011).

Magnesite, hydrous magnesium carbonates, and dolomite samples in this study were dissolved at T_{acid} = 90°C for internal consistency and because the reaction in phosphoric acid is slow at 25°C. The temperature difference of acid digestion thus requires an acid fractionation correction applied to the raw measurements relative to 25°C (by convention, Δ_{47} measurements are reported relative to values obtained by acid digestion at 25°C). Therefore, we compare the measured acid-uncorrected Δ_{47} values in the CDES of Dennis *et al*., (2011) with the calibration curve of Kluge *et al*. (2015) to assess the acid fractionation correction between 25°C and 90°C relative to calcite. We compare it to the calibration of Kluge *et al*. (2015) because that study contains a large dataset, matches theoretical predictions, and was produced using the same techniques we employed at Imperial College. This approach is further justified as different carbonates exhibit the same Δ_{47}-T_{acid} slope relationship albeit with different intercepts related to phosphoric acid reaction and slightly differing equilibrium constants (Schauble *et al*., 2006; Guo *et al*., 2009; Fernandez *et al.*, 2014; Kluge *et al*., 2015).

The acid fractionation correction specific for magnesite and hydrous magnesium carbonates was evaluated using select samples of known temperature of crystallization (Table 1). The samples, highlighted in Table 1, include: (*1*) hydromagnesite from the Red Mountain mine adit (Section 2.3; sample *DP12-10-crust* at 11.3°C); (*2*) synthetic magnesite from olivine dissolution (Section 2.5; samples *0209* and *1210P* at 60°C); (*3*) synthetic hydromagnesite (Section 2.6; samples *Mg-1* and *Mg-3* at 79.9 ± 0.5°C); and (*4*) metamorphic magnesite (Section 2.4.1; sample *14-05 Red* at 450°C; thermodynamic field of stability of the mineral assemblage talc-dolomite-magnesite). In addition, we included select magnesite samples from Falk and Kelemen (2015) with well-constrained formation temperatures to increase the number of samples from six to twelve. Uncorrected acid fractionation Δ_{47} values in the CDES scale were calculated for the data of Falk and Kelemen (2015) by determining first the scaling factor for transfer into the CDES (ratio of columns *T* (values in 10^6T^{-2}) and *R* ($\Delta_{47,ARF}$ in ‰) in the supplementary data file of Falk and Kelemen (2015) and then by applying such scaling factor to the acid-

476 uncorrected Δ_{47} value (column Q in ‰). Falk and Kelemen (2015) assumed an almost
477 identical value for Carrara Marble (0.395 ‰ after acid correction, see Table S3 in their
478 supplementary). Our value for Carrara Marble after acid correction was 0.386-0.389 ‰
479 for different run periods and mass spectrometer (Kluge and John, 2015).
480 The values of the acid fractionation corrections for magnesite and hydrous
481 magnesium carbonates (marked samples in Table 1) were calculated using the
482 unweighted arithmetic mean of the difference between measured raw Δ_{47} values (n=6)
483 and the calcite calibration of Kluge *et al.* (2015) (Equation 3). The uncertainty of the
484 calcite calibration was not taken into account. The resulting acid fractionation correction
485 for combined magnesite and hydrous magnesium carbonate samples with known growth
486 temperature from this study is 0.062±0.021‰ (n=6). Including the raw data of Falk and
487 Kelemen (2015) (n=6) in the calculation of the acid-reaction yields a value of
488 0.070±0.033‰ (n=12), within error of the average from the samples analysed here.
489 Separating the samples into magnesite and hydromagnesite also produces similar results
490 for both groups (0.072±0.038‰ and 0.064±0.022‰, respectively). Consistent with the
491 findings for $CaCO_3$ polymorphs, carbonate-bearing apatite, siderite, and dolomite
492 (Wacker *et al*., 2014; Defliese *et al*., 2015; Eagle *et al*., 2011; Fernandez *et al*., 2014;
493 Kluge and John, 2015), we find no significant difference between the acid fractionation
494 correction for magnesite or hydromagnesite. Most experimentally determined acid
495 fractionation values range from 0.07 to 0.09 ‰ (*e.g*., Passey and Henkes, 2012; Henkes
496 *et al*., 2013; Wacker *et al*., 2013; Defliese *et al*., 2015) and cannot be distinguished from
497 each other with the currently available data and measurement precision. Therefore, in the
498 absence of more precise values we apply the same acid-fractionation correction of
499 0.069‰ as in the study of Kluge *et al*. (2015). For dolomite samples we used the acid
500 correction as for calcite (0.069‰) following Defliese *et al*. (2015).
501 The results of this approach are shown in Figure 8, where the acid fractionation-
502 corrected Δ_{47} values of the experimental and natural magnesite or hydrous magnesium
503 carbonate samples randomly scatter around the calibration curve of Kluge *et al.* (2015) as
504 defined by Equation 4. Our results suggest that an acid fractionation correction of
505 0.069‰ can be applied to magnesite and hydrous magnesium carbonates and that the
506 combined effects of differences in mineral structures and fractionation seem not to result
507 in distinct acid fractionation between magnesium carbonates and other carbonate
508 systems. The samples used for assessing the suitability of the acid-fractionation
509 correction for magnesium carbonates (highlighted in Table 1 and shown in Fig. 8) have
510 also been acid-corrected to 0.069‰ (Table 2) and are henceforth treated as the rest of the
511 samples.
512
513 ***4.2 Magnesium carbonate clumped thermometry***
514
515 Clumped-isotope temperatures of natural and experimentally produced
516 magnesium carbonates were calculated using the acid-corrected Δ_{47} values following the
517 calibration of Kluge *et al*. (2015) (*cf.* Equation 4) and are given in Table 2. The Δ_{47} values
518 and clumped-isotope temperatures for cryptocrystalline magnesite and hydrous
519 magnesium carbonates are shown in detail in Figure 9a. Computed clumped-isotope
520 temperatures for cryptocrystalline magnesite from Red Mountain (California) range from
521 15.9 to 31.6°C, with a mean of 23.3 ± 5.8°C. Austrian magnesite (Kraubath deposit)

records a temperature of 28.2 ± 2.5°C; Turkish (Tutluca deposit) magnesite yields 24.0 ± 5.2°C; and Iranian (Derakht-Senjed deposit) magnesite yields 21.7 ± 8.0°C. Hydrous magnesium carbonates sampled from surface rocks along the 400-km latitudinal transect in California preserve temperatures between 14.2 to 22.7°C, and average 20.0 ± 3.9°C. Mine adit carbonate sample *DPT12-10-crust* (hydromagnesite, minor dypinguite), which was used for the acid fractionation calculation (Section 4.1), exhibits a mineralization temperature of 16.7 °C ± 1.5°C, whereas coexisting *DPT12-10-salt* (nesquehonite) (not used in the acid correction calibration) yielded an anomalous mineralization temperature of 40.2 ± 3.8°C (Fig. 9a) .

Figure 9b displays the high-temperature metamorphic carbonate samples as well as the low-temperature carbonates shown in Figure 9a. High-temperature magnesite (Isua, Greenland), which was used for the acid fractionation calculation (Section 4.1), has a clumped-isotope temperature of 490°C (+60, −40 °C), whereas coexisting dolomite has a temperature of 326 ± 20°C. High-temperature dolomite (Vermont) records a clumped-isotope temperature of 360°C (+70, −50°C) (Fig. 9b). Temperature uncertainties for the high-temperature samples are asymmetrically distributed because the Δ_{47}-T curve is less steep in comparison to low-temperature samples, which results in lower temperature uncertainty for the same Δ_{47} measurement error.

4.3 Calculated $\delta^{18}O$ composition of magnesite and dolomite mineralizing fluids

$\delta^{18}O_{carbonate}$ and $\delta^{13}C_{carbonate}$ values of all natural samples are presented in Table 2 and displayed in Figure 10a relative to the Vienna Standard Mean Ocean Water (VSMOW) and Vienna Pee Dee Belemnite (VPDB), respectively. Computed oxygen isotope ratios of mineralizing fluids ($\delta^{18}O_{fluid,}$ VSMOW) in equilibrium with cryptocrystalline magnesite, hydrous magnesium carbonates, and high-temperature carbonate samples are presented in Table 3 and plotted in Figure 10b. The $\delta^{18}O_{fluid}$ compositions were calculated using the corresponding clumped-isotope temperature of each carbonate (Table 2) and applying the fractionation equations for H_2O-magnesite and H_2O-hydromagnesite reported by Aharon (1988). We adopt the H_2O-magnesite oxygen isotope exchange of Aharon (1988) calibrated with dolomite data (magnesite 2 in Aharon, 1988) to facilitate comparison with other deposits as it has been widely applied to the study of cryptocrystalline magnesite, and reconciles experimental data (based on dolomite) with theoretical predictions for the H_2O-magnesite system (Fig. A6). Additional H_2O-magnesite, H_2O-hydromagnesite, and H_2O-dolomite fractionation equations are summarized in Table A2 and shown for comparison in Fig. A6 (O'Neil and Barnes, 1971; Matthews and Katz, 1977; Aharon, 1988; Vasconcelos *et al*., 2005; Chacko and Deines, 2008). We include these calibrations because there are no experimental data on oxygen isotope fractionation for the H_2O-magnesite system. We note that the oxygen isotope exchange equations of Aharon (1988) and O'Neil and Barnes (1971) are internally consistent, closely resemble experimental data, and yield $\delta^{18}O_{fluid}$ compositions that correspond to possible natural fluid sources. Fig. A6 highlights the clustering of the oxygen isotope exchange equations available for dolomite, magnesite, hydromagnesite, and calcite. We find that using the H_2O-magnesite equation of Chacko and Deines (2008) results in much lower $\delta^{18}O_{fluid}$ compositions that do not match the oxygen isotope composition natural waters. For example, the corresponding

$\delta^{18}O_{fluid}$ values for Red Mountain magnesite using Chacko and Deines (2008) would range from −10.4 to −14.8‰, which are values seldom described for California. The $\delta^{18}O_{fluid}$ composition in equilibrium with metamorphic dolomite (Isua, Greenland and Vermont) was determined using the dolomite calibration of Vasconcelos *et al*. (2005).

As shown in Figure 10b, the Red Mountain (California), Austrian, Turkish and Iranian cryptocrystalline magnesite samples have $\delta^{18}O_{fluid}$ compositions within the range of present-day meteoric fluids. Similarly, hydrous magnesium carbonates collected from surface exposures exhibit a range in $\delta^{18}O_{fluid}$ values consistent with meteoric water in coastal California. In contrast, the coexisting high-temperature magnesite and dolomite (Isua, Greenland), and dolomite (Vermont) fall within the $\delta^{18}O_{fluid}$ composition range of metamorphic/connate fluids.

4.5 Calculated $\delta^{13}C$ composition of mineralizing carbonate species, $CO_{2\ (g)}$

Computed $\delta^{13}C$ values of $CO_{2(g)}$ in equilibrium with the carbonates ($\delta^{13}C_{CO2(g),}$ VPDB) are given in Table 3 and shown in Figure 10b. The $\delta^{13}C_{CO2(g)}$ values are calculated based on the expanded equation of Aharon (1988), which is applicable for both dolomite and magnesite:

$$\delta^{13}C\ (CO_{2(g)}) = \delta^{13}C_{carbonate} - 3.168(10^6/T^2) + 7.6663(10^3/T) - 2.6312 \qquad (5)$$

where T is the clumped-isotope temperature in K (Table 2) and $\delta^{13}C_{carbonate}$ is the measured carbon isotope composition (Tables 2 and 3). Although other magnesite-$CO_{2(g)}$ fractionation relationships exist (Fig. A7; Golyshev *et al.* (1981) and Chacko and Deines (2008), we apply Aharon (1988) for internal consistency and because it is based on data and calculations used to derive the widely used H_2O-magnesite relationship described in Section 4.4.

Figure 10b shows the calculated $\delta^{13}C_{CO2(g)}$ values for California (Red Mountain), Austrian, Turkish, and Iranian cryptocrystalline magnesite, which exhibit values that broadly correspond to $\delta^{13}C$ compositions of organic sources (plant CO_2, soil, petroleum) and carbon contained in silicate and oxide minerals that constitute representative ultramafic rocks (*i.e.* non-carbonate CO_2 in Fuex and Baker, 1973). Additionally, hydrous magnesium carbonates from surface exposures in California display a range in $\delta^{13}C$ ($CO_{2(g)}$) that also coincides with that of cryptocrystalline magnesite. In contrast, mine adit precipitates show correlation with modern-day values of atmospheric CO_2. High-temperature magnesite and dolomite (Isua, Greenland), and dolomite (Vermont) have corresponding $\delta^{13}C_{(CO2(g))}$ compositions of magmatic origin (Fig. 10b and Table A5).

4.6 Evaluation of clumped-isotope temperatures and $\delta^{18}O$ and $\delta^{13}C$ compositions relative to geological constraints

4.6.1 Red Mountain (California) cryptocrystalline magnesite

Samples of cryptocrystalline magnesite from Red Mountain yield temperatures in the range of 15.9 to 31.6 °C with a mean value of 23.3 ± 5.8 °C (Table 2; Figs. 9a and 11). These temperatures are lower than typical serpentinization temperatures in

614 continental settings (85-115 °C in chrysotile-lizardite mineralogies; Wenner and Taylor,
615 1971), in agreement with the observation that magnesite vein mineralization postdates
616 serpentinization in the host peridotite rock. The calculated $\delta^{18}O_{fluid}$ composition of the
617 fluid in isotopic equilibrium with Red Mountain cryptocrystalline magnesite (between
618 −6.8 and −11.2 ‰; Table 3 and Fig. 10b) is broadly consistent with the composition of
619 spring, river, and meteoric waters local to the Del Puerto peridotite area (−7.1 to −8.7 ‰)
620 (Barnes and O'Neil, 1969; Blank *et al*., 2009), and the annual mean rainfall $\delta^{18}O$ value in
621 California (−6 and −10 ‰; Kendall and Coplen, 2001). Although these results suggest a
622 dominating influence of surface meteoric waters in the magnesite mineralization process,
623 our data do not categorically rule out sourcing from and mixture of fluids of different
624 $\delta^{18}O_{fluid}$ compositions. For example, California oil-field waters and connate/metamorphic
625 fluids range from −8.14 to +5.93 ‰ (White *et al*., 1973) and are hosted in sedimentary
626 and metasedimentary units of the Franciscan Formation and the Great Valley Sequence,
627 which underlie and are in tectonic contact with the Del Puerto ophiolite and peridotite.
628 The relatively enriched metamorphic waters in the California Coast Ranges have a $\delta^{18}O$
629 of 7‰ (Barnes *et al.*, 1973), which constrains the $\delta^{18}O$ value of possible fluids at Red
630 Mountain to between −8.7 and 7 ‰. Using the $\delta^{18}O$ value (3.14 ‰) of waters hosted in
631 the Franciscan Formation (Barnes *et al.*, 1973), we obtain a mixture of up to 84±14 %
632 meteoric water and 16±14 % Franciscan Formation water. The Red Mountain magnesite
633 deposit is likely a system dominated by meteoric waters that potentially exchanged with
634 fluids from the underlying rocks, namely the Franciscan Formation and the Great Valley
635 Sequence. Such a model may be correlative with the proposed near-surface epithermal
636 model of Pohl (1990) for the formation of cryptocrystalline magnesite deposits.
637
638 *4.6.2 Austrian magnesite (Kraubath)*
639
640 The Kraubath magnesite, the classic locality for cryptocrystalline magnesite in
641 Austria (Redlich, 1909; Kralik *et al*., 1989; Zachmann and Johannes, 1989; Horkel *et al*.,
642 2009), exhibits a formation temperature of 28.2 °C. This temperature is much lower than
643 the previously suggested limit of 80 °C for the deposit (Ece *et al*., 2005), but it is
644 consistent with the temperature range between 13 and 42 °C proposed by Kralik *et al*.
645 (1989) (Table A1 and Fig. 11). Using the clumped-isotope temperature, the calculated
646 mineralizing $\delta^{18}O_{fluid}$ composition is –9.1 ‰, which is virtually identical to present-day
647 surface waters in Austria (–8.6 to –8.7 ‰; Kralik *et al*., 1989) and consistent with
648 historical $\delta^{18}O_{fluid}$ compositions of meteoric water in Austria (–14.29 to –6.23 ‰;
649 IAEA/WMO, 2015; Fig. 10b and Table A5).
650
651 *4.6.3 Turkish magnesite (Tutluca open pit, Eskisehir, Turkey)*
652
653 The clumped-isotope temperature for Tutluca magnesite is 24.0 °C, lower than
654 estimated using conventional oxygen isotope thermometry for the Tutluca deposit with
655 37.9 °C (Kahya and Kuşcu, 2014) and other large magnesite vein complexes in Turkey at
656 ~80 °C (Zedef *et al.*, 2000; Table A1 and Fig. 11). Our temperature places the
657 mineralizing $\delta^{18}O_{fluid}$ composition at –9.4 ‰, depleted with respect to the modern
658 meteoric water oxygen isotope composition (–5.0 ‰) assumed for the Turkey (used by
659 Kahya and Kuşcu (2014), reported by Zedef *et al*., 2000), but consistent with

representative freshwater springs and lakes in Turkish basins (~ –5.4 to –12.0 ‰; Leng and Marshall, 2004) and within the range of historical $\delta^{18}O_{fluid}$ compositions of meteoric water in Turkey (–11.22 to –3.61 ‰; IAEA/WMO, 2015; Fig. 10b and Table A5).

4.6.4 Iranian magnesite (Derakht-Senjed, Iran)

Iranian magnesite from Derakht-Senjed records a clumped-isotope temperature of 21.7 °C, indicating equilibrium from a fluid with $\delta^{18}O_{fluid}$ of –13.95 ‰, which is depleted with respect to reported $\delta^{18}O_{fluid}$ of stream waters in Iran (–4.43 to –3.45 ‰; Mirnejad *et al.*, 2008), but in agreement with the range of precipitation representative of Iran that can reach values of ~ –15 ‰ (IAEA/WMO, 2015; Fig. 10b and Table A5). Our clumped-isotope temperature data suggest that Derakht-Senjed magnesite formed at shallow depths and at low temperature, in agreement with the other cryptocrystalline magnesite deposits examined in the present study and with other Iranian magnesite deposits where the range of mineralization temperatures is thought to be between 20 and 44 °C (Table A1 and Fig. 11; Mirnejad *et al*., 2008).

4.6.5 Hydrous magnesium carbonates (California Coast Ranges)

Hydrous magnesium carbonates from surface exposures in the California Coast Ranges preserve clumped-isotope temperatures between 14.2 to 22.7 °C (Fig. 9a). These temperatures coincide with the maximum monthly average temperatures for each location at the onset (October) and culmination (April-May) of the rainy season in California (Figs. A4-A5). McLaughlin hydromagnesite, the northernmost sample (Fig. 1b), preserves a clumped-isotope temperature of 22.7 °C, which is typically reached at the beginning of the rainy season in October and at its end in April (Fig. A4a-A4b). Although temperatures of ~22.7 °C are exceeded during the summer months (May to September), the lack of rain and low humidity during those months are likely unfavorable for the formation of hydromagnesite at the surface (Fig. A4b). Similarly, hydromagnesite at Del Puerto likely precipitates in October-November or February-April when the clumped-isotope temperature (14.2°C) coincides with the maximum daily temperatures (Figs. A4c-A4d and A5). Artinite and hydromagnesite from New Idria, the southernmost samples, precipitate exclusively in the rainy season that begins in October and extends to May (Fig. A4e-A4f). Our observations are comparable with the seasonality of carbonate soil and paloesol formation determined in other climatic zones, including Arizona, Nevada, Tibet, Pakistan, and India (Quade *et al*., 2013) and New Mexico (Breecker *et al*., 2009). The clumped-isotope temperatures determined for hydrous magnesium carbonates corroborate the dependence on seasonality (*i.e.* coupled temperature and water supply) in the formation of hydrous magnesium carbonates prevalent in the Mediterranean climate (*Csa*, Köppen climate classification system; Kesseli, 1942; Kauffman, 2003) of the California Coast Ranges.

Calculated $\delta^{18}O$ compositions of water in equilibrium with hydrous magnesium carbonates span from −4.7±0.1 ‰ at McLaughlin, to −5.8±0.2 ‰ at Del Puerto, and to −6.5±0.1 ‰ (hydromagnesite and artinite) at New Idria. These compositions agree with the modern range of meteoric water $\delta^{18}O$ compositions for California (*cf.* White *et al*., 1973; Barnes *et al*., 1973; Kendall and Coplen, 2001; Blank *et al*., 2009).

Hydromagnesite samples in close contact with soil profiles and vegetation (Fig. 4a, McLaughlin *MCL-2*; Fig. 4c, Del Puerto *RC1*; Fig. 4e, New Idria *09-NI-3*) exhibit more depleted values in $\delta^{13}C$ (up to −13.69 ‰; Table 2) with respect to artinite (Fig. 4f, *10-NI-1*; −5.69 ‰, Table 2) that is away from biogenic sources of CO_2 and was collected from an isolated pool of shallow water. The corresponding values of $\delta^{13}C_{CO2(gas)}$ for hydromagnesite range between −34.0 and −26.2 ‰, which suggests the strong input of biogenic CO_2 derived from C_3 plants ($\delta^{13}C$ <−24 ‰; Fig. 10b; *e.g.,* Oskierski *et al.*, 2013). The calculated value of $\delta^{13}C_{CO2(gas)}$ for New Idria artinite (−18.5 ‰) is less depleted with respect to the hydromagnesite samples and points to a higher input of atmospheric CO_2 for mineralization ($\delta^{13}C$ ~ −6 ‰; Fig. 10b). The $\delta^{13}C$ composition of hydrous magnesium carbonates probably preserves the biological signature of endemic and often unusual ultramafic/serpentine C_3 flora, which includes trees and shrubs, herbaceous perennials and annuals in a combination of chaparral and grassland ecosystems (Kruckeberg, 1992; Harrison *et al*., 2006).

4.6.6 Mine adit hydrous magnesium carbonates (Red Mountain mine)

The hydromagnesite-dypingite sample (*DPT12-10 Crust*) from Red Mountain yields a temperature of 16.7 ± 1.5 °C (Table 2; Fig. 9a), which is broadly consistent with the expected temperature constrained by the temperature at the mine of 11.3 °C (Fig. 5a). In turn, disequilibrium effects are evident in the relatively lower Δ_{47} values in the nesquehonite *(DPT12-10 Salt*) that translate to a temperature of 40.2 ± 3.8 °C (Table 2; Fig. 9a). Infiltrating water that coats the surface adit walls and ceilings controls the formation of these carbonates. Airflow and circulation at 200 m from the adit entrance are very limited (Fig. 5a), but sufficient to exchange with atmospheric CO_2 through the adit entrance; however, temperatures of ~40 °C are never reached within the mine. The loss of accumulated dissolved inorganic CO_2 while alkalinity is maintained in thin water films and droplets results in supersaturation and precipitation of abundant crustiform hydromagnesite-dypingite, followed by nesquehonite. Textural differences suggest that the hydromagnesite-dypingite and nesquehonite represent different episodes of carbonate precipitation on the adit walls (Fig. 5a-c). We address the anomalously high mineralization temperature of nesquehonite *(DPT12-10 Salt*) in Section 5.4.

4.6.7 Dolomite and magnesite in talc-carbonate veins, Isua (Greenland)

Measured values of Δ_{47} in cogentic magnesite (sample *14-05 Red*) and dolomite (sample *14-05 White*) from the Isua Supracrustal Belt (ISB), Greenland are 0.326 and 0.358 ‰, and correspond to temperatures of 490 (+60 °C, −40 °C) and 326 ± 20 °C, respectively (Fig. 9b; Table 2). The calculated clumped-isotope temperature of magnesite (490 °C) is consistent with theoretical predictions of metasomatism and alteration of ultramafic rocks in Isua, whereas the coexisting dolomite preserves a temperature that is ~165°C lower. The clumped-isotope temperature of Greenland dolomite represents the blocking temperature rather than formation temperature (see Section 5.5). Using the clumped-isotope temperature for magnesite, the $\delta^{18}O_{fluid}$ of the mineralizing fluid was +4.6 ‰, which is a representative composition consistent with fluids of metamorphic origin (range +3 to +20 ‰; Sheppard, 1986; Fig. 10b; Table A5). The $\delta^{13}C_{mag}$ and $\delta^{13}C_{dol}$

values are virtually identical, −3.2 and −3.3 ‰, respectively, and consistent with other reported metacarbonates in Isua that range in $\delta^{13}C$ from ~ −7.6 to −1.1 ‰ (Van Zuilen *et al.*, 2003). The ISB experienced a number of metamorphic events (Nutman *et al.*, 1984; Nutman *et al.*, 1996) and the antigorite+talc+magnesite assemblage is interpreted as representing retrograde metamorphism (Nutman *et al.*, 1996). The talc-carbonate veins crosscut oceanic antigorite (sample *15-05*; Pope *et al.*, 2012), which suggests that the veins postdate serpentinization and are related to mobilization of a late-stage CO_2-rich metamorphic fluids under retrograde conditions.

4.6.8 Dolomite associated with talc-magnesite deposit (Ludlow, Vermont)

Dolomite from Vermont (sample *08SVT-4A*) has a Δ_{47} value of 0.348 ‰ and yields a clumped-isotope temperature of 360 °C (+70 °C, −50 °C; Table 2, Fig. 9b), which is slightly lower than the expected range of alteration (430-490 °C; Table 1). Applying the clumped-isotope temperature of 360 °C (+70 °C, −50 °C), dolomite formed from a fluid with a $\delta^{18}O_{fluid}$ value ranging from 2.3 to 4.5 ‰. However, the clumped-isotope temperature of Vermont dolomite appears to represent a blocking temperature rather than a formation temperature (see Section 5.5), so that the calculated $\delta^{18}O_{fluid}$ values of the mineralizing fluid are relatively lower by 1 ‰. At a temperature of 430 °C (maximum clumped-temperature within error and lower limit of theoretical prediction), the $\delta^{18}O_{fluid}$ value of 4.5 ‰ coincides with the general $\delta^{18}O_{fluid}$ compositional field of metamorphic waters (+3 to +20 ‰; Sheppard, 1986).

The clumped-isotope temperature (360 °C, +70 °C, −50 °C) of Vermont dolomite lies within the range of estimated temperatures (210-550°C) for metamorphic zones in Southeastern Vermont (Sheppard and Schwarcz, 1970). However, measured $\delta^{18}O_{dol}$ (+10.95 ‰) and $\delta^{13}C_{dol}$ (−12.85 ‰) compositions are respectively ~ 2 ‰ and 10 ‰ lower than other dolomite in the area (Sheppard and Schwarcz, 1970). The isotopic compositions of Vermont dolomite probably reflect the influence of the reduced carbonaceous, graphite-bearing sulfidic biotite schist that encloses the host serpentinite and buffers the activity of CO_2 according to water-graphite equilibria (*e.g.* Robinson *et al.*, 2006) and likely supplied CO_2 for carbonate mineralization. Although $\delta^{13}C$ compositions of the graphitic schist surrounding the talc-magnesite-dolomite deposit are not available, graphite in the neighboring Waits River Formation, eastern Vermont, ranges in $\delta^{13}C_{graphite}$ composition from −11.9 to −14.3 ‰ (Stern *et al.*, 1992) and resemble the carbon isotope composition of dolomite at Ludlow. For comparison, metamorphosed sedimentary rocks in Isua, Greenland preserve graphite with compositions between −16 and −9 ‰ in equilibrium with siderite at 400-500 °C (Perry and Ahmad, 1977).

5. Discussion

Most natural and synthetic carbonates precipitate at or near homogenous isotope exchange equilibrium with respect to the carbonate ion contained in the mineral phase (*cf.* Equation 2 and Fig. A2) (*e.g.*, Eiler, 2011) and yield clumped-isotope temperatures generally consistent with expected formation temperatures (*e.g.*, Eiler *et al.*, 2014). Notable exceptions include speleothems (Kluge and Affek, 2012; Kluge *et al.*, 2014) and low-temperature corals (Saenger *et al.*, 2012). These exceptions have been explained by

kinetic effects possibly associated with bicarbonate-carbonate (de)hydration and (de)hydroxylation, pH variations, and biologically induced effects. In the case of magnesium carbonates, we explore here additional geologic and experimental constraints that point to both consistent and discrepant values of Δ_{47} and resultant clumped-isotope temperatures.

5.1 Synthetic magnesium carbonates

Perhaps the most significant limitation concerning the application of clumped isotopes to magnesium carbonates is the paucity of data required for robust calibration and standardization of heterogeneous isotope exchange between magnesite and H_2O as well as homogeneous isotope exchange (Equation 2) required for clumped-isotope thermometry. In part, the limitation derives from the difficulty associated with magnesite precipitation from solution at low (<25 °C) and standard ambient temperatures and the propensity to form hydrous magnesium carbonates (*e.g.*, Deelman, 1999; Hänchen *et al*., 2008; Bénézeth *et al.*, 2011). Our data indicate that synthetic hydromagnesite (Section 2.6; samples *Mg-1* and *Mg-3*) yields Δ_{47} values that result in clumped-isotope temperatures (n=2; 79.2 ± 4.6 °C) virtually identical to the known precipitation temperature of 79.9 ± 0.5 °C (Tables 1 and 2; Fig. 11).

In contrast, the magnesite samples produced from dissolution of forsterite in a two fluid phase system (H_2O and CO_2) at 60 °C and 100 bars (samples *0209* and *1210P*) record anomalously high Δ_{47} values (about 0.03 ‰ above the calibration line) that yield clumped-isotope temperatures (n=2; 45.8 ± 6.5 °C) lower by ~15 °C (Table 2 and Fig. 11). These results could be due to (*1*) statistical variability; (*2*) a pH-dependent speciation effect; or (*3*) magnesite formation after the experiment was stopped (during cooling and degassing). The standard error of samples measured in 3-5 replicates is typically 0.015-0.010‰. Thus, the olivine dissolution samples are within 2-3 standard errors of the calibration line. Taking into account the uncertainty of the calibration line, the deviation could be statistically insignificant. On the other hand, pH-dependent speciation of the dissolved inorganic carbonate (DIC) species (*i.e.* H_2CO_3, HCO_3^- and CO_3^{2-}) have a distinct equilibrium clumped-isotope signature (Δ_{47}) that is preserved by the mineral depending on formation conditions (Hill *et al*., 2014). These experiments were maintained at low pH (4.5-5.5) (Johnson *et al*., 2014) and could theoretically be affected by pH-induced disequilibrium in the Δ_{47} values of the DIC pool. Theoretical calculations of Hill *et al*. (2014) suggest that mineral formation at low pH could cause an offset to higher Δ_{47} values on the order of about 0.03 ‰, which results in lower clumped-isotope temperatures. Although this Δ_{47} offset is similar to our measurements (~ 0.03 ‰), pH effects proposed by Hill *et al*., (2014) and Tripati *et al*., (2015) appear not to affect experimentally grown carbonates at pH 8.3-10.5 (Tang *et al*., 2014) and natural travertines at pH 5.6-9 (Kele *et al*., 2015). Because we cannot exclude either the influence of a statistical artifact or possible DIC speciation effects from our analysis, we suggest that either could explain the deviation between measured and expected values. These results reveal the complicated nature of magnesite formation, and emphasize the need for additional multiphase precipitation and dissolution-precipitation experiments and further theoretical and experimental investigations of pH effects in the clumped isotope system. In contrast, carbonates precipitated from solution following recipes from

McCrea (1950) and Kim and O'Neil (1997) used for equilibrium calibrations of clumped-isotope measurements produce consistent results as demonstrated by the hydromagnesite samples (*Mg-1* and *Mg-3*) presented in this study.

5.2 Cryptocrystalline magnesite

Cryptocrystalline magnesite displays a relatively uniform Δ_{47} composition irrespective of the type (nodular, stockwork vein, massive vein) and locality (Table 2). The Δ_{47} compositions yield a clumped-isotope temperature range from 15.9 to 31.6 °C (mean of 23.7 ± 5.0 °C) for the various types and different localities (California, Austria, Turkey, Iran) and are broadly consistent with the clumped-isotope temperatures reported for similar magnesite samples from Oman (Table A1; 23-26 ± 2 °C; n=2; Streit *et al*. 2012) and New Caledonia (Table A1; 26-42 °C; n=7; Quesnel *et al*., 2016). Calculated clumped-isotope temperatures lie in the lower range of temperatures for cryptocrystalline magnesite based on classical oxygen isotope thermometry (range from 10 to 100°C; Table A1 and Fig. 11).

Cryptocrystalline magnesite appears to be a widespread alteration product of dunite, peridotite, and serpentinite related to ophiolite bodies worldwide (Pohl, 1990; Abu-Jaber and Kimberley, 1992b; Schroll, 2002). Genetic models for the formation of ultramafic-hosted cryptocrystalline magnesite proposed to date are varied and appear to be site-specific (Petrov, 1980; Pohl, 1990; Jedrysek and Halas, 1990; Fallick *et al.*, 1991; Abu-Jaber and Kimberley, 1992a; Zedef *et al*., 2000; Ghoneim *et al*., 2003; Gartzos, 2004; Ece *et al*., 2005; Kelemen, 2008; Mirnejad *et al.*, 2008; Jurković *et al*., 2012; Streit *et al*., 2012; Oskierski *et al.*, 2013; Quesnel *et al*., 2013; Kahya and Kuşcu, 2014; Ulrich *et al*., 2014; Quesnel *et al*., 2016), and largely depend on stable carbon and oxygen isotope compositions. Based on structural relationships, the serpentinization of peridotite at each deposit is a result of tectonic and geochemical processes that appear to restrict the formation of cryptocrystalline magnesite to upper crustal levels after serpentinization. In general, cryptocrystalline magnesite exhibits $\delta^{18}O_{mgs}$ compositions from >22 to 40 ‰ and $\delta^{13}C_{mgs}$ values between −21.0 and −4 ‰ (Table A3; Fig. 10a; Kralik *et al*., 1989; Oskierski *et al.*, 2013), consistent with the compositions reported here (Table 2 and Fig. 10a). These relatively large ranges in stable isotope values, along with structural observations, have led to at least two end-member models of cryptocrystalline magnesite mineralization in ultramafic rocks.

Cryptocrystalline magnesite has been inferred to form as the result of either supergene or hydrothermal mineralization processes, or a combination of both. Supergene models assume dissolution and leaching of ultramafic rocks in weathering zones, where infiltrating meteoric waters transport magnesium and biogenic- and atmospheric-derived CO_2, precipitating magnesite at low temperatures. The cryptocrystalline morphology and the discrete presence of shrinking or dehydration cracks have been interpreted to represent supergene mineralization of hydrous magnesium carbonates as precursors to cryptocrystalline magnesite (Lesko, 1972). Although some magnesite deposits are clearly associated with laterite weathering zones (Quesnel *et al.*, 2013), most magnesite deposits do not occur in close relation to laterites (Pohl, 1990). In contrast, a hydrothermal origin requires moderate to higher temperatures to provide conditions for the release of mineralizing CO_2 (*e.g.*, via decarboxylation and decarbonation reactions during thermal

contact metamorphism; Zedef *et al.*, 2000). Genesis in hydrothermal environments also requires the creation of large open volume space and/or a fracturing mechanism to form large magnesite veins (maximum vein thickness ~45 m (Mantudi/Euboea, Greece; Pohl, 1989; Pohl, 1990); and Red Mountain magnesite ~36 m) and the possible coupled tectonic and syn-deformation filling of tensional structures (Quesnel *et al*., 2013). The wide range of $\delta^{18}O_{mgs}$ and $\delta^{13}C_{mgs}$ compositions of worldwide magnesite also suggests a variety of sources of water and CO_2, and variable water/rock ratios. Because hypogene, hydrothermal, and connate fluids can be of meteoric origin (Kelemen and Matter, 2008; Carreira *et al*., 2008; Kelemen *et al.*, 2011), discriminating between two modes of magnesite formation may not be possible without additional field-specific constraints.

Figure 10a shows measured $\delta^{18}O_{mgs}$ and $\delta^{13}C_{mgs}$ compositions of cryptocrystalline magnesite from this study (California, Austria, Turkey and Iran; Table 2) juxtaposed with the $\delta^{18}O_{mgs}$ and $\delta^{13}C_{mgs}$ compositional fields of additional worldwide cryptocrystalline magnesite deposits (Compilation data and references in Table A4). Additionally, according to Figure 10b, discerning the source of the CO_2 for each specific cryptocrystalline magnesite deposit will require detailed appraisal of the local sources of CO_2 in each deposit. For example, the $\delta^{13}C_{mgs}$ compositions of the mineralizing CO_2 are typically within a range associated with biogenically processed carbon, including hydrocarbons (petroleum) or a mix of plant-derived inputs. In contrast, the computed $\delta^{18}O_{fluid}$ values of the mineralizing fluid for cryptocrystalline magnesite reflect in large part the isotopic compositions of meteoric water representative for each area (Sections 4.6.2, 4.6.3 and 4.6.4). Although cryptocrystalline magnesite deposits presented here are disseminated with respect to geologic setting and time, the restricted range of Δ_{47} compositions and resulting temperatures could indicate a relatively consistent set of geologic processes that lead to the formation of cryptocrystalline magnesite in serpentinized peridotite rocks. Our clumped-isotope data indicate that percolation and mixing of meteoric surface waters to form the cryptocrystalline magnesite deposits worldwide are typical for large-scale carbonation of ultramafic rocks.

The formation of cryptocrystalline magnesite by meteoric fluids does not imply that other geologic processes can be excluded, particularly those that help explain the morphology and size of the veins, or the intense brecciation that often accompanies magnesite deposits. For example, Quesnel *et al.* (2013) proposed that active tectonics play a role in the formation of large volumes of cryptocrystalline magnesite. Although it is possible that cryptocrystalline magnesite may form in disequilibrium with the mineralizing solution, so far the maximum isotopic disequilibrium that yields lower than expected temperatures in carbonates is recorded in surface corals at ~10 °C (Eiler *et al*., 2014) and the olivine-magnesite experiments at ~15 °C, which may exhibit pH disequilibrium effects (Section 5.1). Even if a similar enrichment mechanism of ^{13}C-^{18}O bonds were operative during the formation of cryptocrystalline magnesite, which would yield anomalously cold temperatures, it would have to be an extreme effect that yields a temperature difference far greater than 10 °C. Such effect has been documented in rapid carbonate precipitation in high pH solutions (Schmid, 2011). It is assumed that cryptocrystalline magnesite precipitates from a solution *sensu stricto*, but textural evidence has been interpreted to indicate an origin from a colloidal solution or as gel (Bodenlos, 1950; Pohl, 1990) as implied by its name, *gel magnesite* (see textures in Figs. 2a-2c). In this case, materials such as cryptocrystalline magnesite derived from colloidal

solutions or as gels may preserve unique clumped-isotope compositions (Δ_{47}) and thus anomalous resultant temperatures. Colloidal solutions and gels have unique geochemical characteristics (*e.g.* high surface area, irregular electric surface charge and ion exchange potential, anomalous water properties; Brinker and Scherer, 1990) that could cause significant effects on stable and clumped isotope systematics on both the solution and resultant crystalline material. The relatively low clumped-isotope temperature (23.7 ± 5.0 °C; range from 15.9 to 31.6 °C) points to a long-lived interaction with relatively cold meteoric water, which constitutes either the mineralizing fluid itself or an overprinting fluid that exchanges isotopically with cryptocrystalline magnesite or drives recrystallization. In the latter cases, the ensuing isotope-exchange reactions could occur at the surface of the highly porous (high surface area) cryptocrystalline magnesite (Figs. 2a-2c) or promote partial to full dissolution and recrystallization, as suggested for marine carbonates (Maher *et al*., 2006; Fantle *et al*., 2010) and experimental studies of C and Mg isotope exchange between hydromagnesite and the co-existing fluid (Mavromatis *et al*., 2012; Mavromatis *et al*., 2015). Hence, we cannot categorically rule out the possibility that cryptocrystalline magnesite may have been emplaced at higher temperatures and overprinted by fluids to record <31.6°C (average 23.7 ± 5.0°C) clumped-isotope temperatures (Fig. 11). In either case, the influence of meteoric water in mediating the formation of cryptocrystalline magnesite worldwide deposits is unequivocal.

5.3 Hydrous magnesium carbonates (California Coast Ranges)

Surface hydrous magnesium carbonates from the California Coast Ranges preserve clumped-isotope temperatures between 14.2 to 22.7 °C (Fig. 9a), consistent with the maximum monthly average temperatures for each location at the onset (October) and culmination (April-May) of the rainy season in California (Fig. A4-A5). We infer that nucleation and growth of hydrous magnesium carbonate phases in the California Coast Ranges occur due to two synchronous processes: when surface waters permeate the sheared serpentinite and serpentinized peridotite during the period of October-April and surface temperatures reach values between 14 to 23 °C, as determined by clumped-isotope temperatures.

Clumped-isotope temperatures for hydrous magnesium carbonates in California are consistent with thermodynamic calculations and phase relations estimated for artinite and hydromagnesite. Artinite is stable at lower pCO_2 than hydromagnesite (Dandurand and Schott, 1977) and because very small nodules of hydromagnesite develop along the artinite fibers (see Cisneros 1977), we suggest that the New Idria artinite forms along the stability field of both hydromagnesite and artinite at $log(pCO_2[bars])$ of −6 to −5 (Dandurand and Schott, 1975; Königsberger *et al*., 1999). Similarly, using the clumped-isotope temperatures for McLaughlin and New Idria hydromagnesite at 22.7 and 21.1°C, respectively, hydromagnesite stability occurs between $log(pCO_2[bars])$ of −5 to −3 (Dandurand and Schott, 1975; Königsberger *et al*., 1999). Although hydromagnesite is considered to be a metastable phase that transforms to magnesite (Bénézeth *et al*., 2011), we found no textural or crystallographic evidence of cogenetic magnesite in the hydrous magnesium carbonates.

Clumped-isotope temperatures and stable isotope compositions of hydrous magnesium carbonates record the effect of local latitudinal variations along the central

portions of the California Coast Ranges. The relatively low $\delta^{13}C$ values for hydrous magnesium carbonates reflect the incorporation of biogenic CO_2 (Fig. 10b). Calculated $\delta^{18}O_{fluid}$ compositions (−4.7±0.1 ‰ at McLaughlin; −5.8±0.2 ‰ at Del Puerto; and −6.5±0.1 ‰ at New Idria; Table 3) agree with the range of meteoric water $\delta^{18}O$ compositions for California (Fig. 10b; *cf.* White *et al*., 1973; Barnes *et al*., 1973; Kendall and Coplen, 2001; Blank *et al*., 2009) and exhibit relative depletion in ^{18}O from north to south. A similar trend of variability of isotope composition as a function of latitude is also observed in the measured $\delta^{2}H$ values of the hydrous magnesium carbonates, where relatively less depleted $\delta^{2}H$ are recorded at McLaughlin (−122.9 ± 1.4‰), and become increasingly depleted to the south, such that $\delta^{2}H$ at Del Puerto is −129.9 ± 1.3‰, and −132.0 ± 1.3‰ at New Idria (Table A6; Methods for $\delta^{2}H$ measurements in Appendix B). Calculated mineralizing $\delta^{18}O_{fluid}$ and $\delta^{2}H$ values of hydrous magnesium carbonates decrease with decreasing latitude. This observation is best explained by local meteorological conditions related to latitudinal variations along the central portions of the California Coast Ranges (Fig. 1B). Hydrous magnesium carbonates form at relatively similar elevations (Table S3) and are effectively at the same distance from the Pacific Ocean (Fig. 1B), minimizing topographic and 'continental effects' (Poage and Chamberlain, 2001; Breecker et al., 2009; Mix et al., 2011; Winnick et al. 2014). Latitude effects appear to influence the isotopic composition of mineralizing meteoric waters and resultant hydrous magnesium carbonates along the California Coast Ranges. In this case, clumped-isotope temperatures offer a means for calculating the $\delta^{18}O_{fluid}$ compositions of precipitation and surface waters, extending the use of clumped-isotope thermometry to help discern factors controlling the isotopic composition of fluids in continental settings.

5.4 Mine adit hydrous magnesium carbonates (Red Mountain mine)

Hydromagnesite+dypingite (sample *DPT12-10-crust*) from the Red Mountain adit yields a temperature of 16.7 ± 1.5 °C that is broadly consistent with inferred mine adit temperature (11.3 °C). In contrast, disequilibrium effects are evident in the relatively lower Δ_{47} values of the nesquehonite (sample *DPT12-10-salt*) that translate to an apparent temperature of 40.2 ± 3.8 °C (Table 2; Fig. 9a). The main difference between crustiform hydomagnesite-dypingite and nesquehonite appears to be the timing of mineralization, whereby the last episode of mineralization (nesquehonite) reflects progressive evaporation that promotes nesquehonite saturation via CO_2 degassing in the water-rich droplets, which are the last and longer-lived features of a moist adit wall. Degassing of CO_2 mediates carbonate precipitation in thin films to form speleothems (Buhmann and Dreybrodt, 1985; Dreybrodt, 1999) and can result in substantial kinetic effects in clumped-isotope compositions, consistent with similar observations in calcium carbonates in caves (Affek *et al*., 2008; Daëron *et al*., 2011; Kluge and Affek, 2012; Kluge *et al*., 2013; Affek *et al*., 2014) and experimental analogs (Affek and Zaarur, 2014). Comparable to calcium carbonate speleothems, nesquehonite records clumped-isotope compositions that result in anomalously warmer temperatures related to kinetic factors associated with dehydroxylation (Eiler *et al.*, 2014) or dehydration (Affek and Zaarur, 2014) of HCO_3^- and ensuing CO_2 degassing. Such effects are also recognizable in the enrichment by ~3.3‰ in the $\delta^{13}C$ compositions ($\delta^{13}C$ of hydromagnesite+dypingite is 3.94‰ and nesquehonite is 7.31‰; Table 2). Similar kinetic effects have been reported

for hydrous magnesium carbonate mine adit coatings (*e.g.*, lansfordite, $MgCO_3 \cdot 5H_2O$) in subarctic conditions (Beinlich and Austrheim, 2012). We rule out the possibility of microbial mediation in mine adit magnesium carbonate precipitation and therefore "vital effects" in the isotopic and clumped-isotope compositions because evidence of microbial activity (*e.g.*, microbial mats, mucous biofilms or microbialites) is not present (Fig. 5).

5.5 High temperature metamorphic magnesium carbonates

Measured values of Δ_{47} in magnesite from the Isua Supracrustal Belt (ISB), Greenland correspond to temperatures of 490 °C (Fig. 9b; Table 2), whereas the coexisting dolomite records a temperature of 326 °C. Only magnesite reproduces clumped-isotope temperatures in agreement with theoretical predictions of metasomatism and alteration of ultramafic rocks in Isua (*cf.* Section 2.4.1). The discrepancy in clumped-isotope temperatures between the two carbonate phases appear to be related to differences in apparent equilibrium blocking temperature in relation to ^{13}C-^{18}O bond reordering.

The apparent equilibrium blocking temperature refers to the measured Δ_{47} value and clumped-isotope temperature where the internal reordering of the isotope-exchange reaction, as expressed in Equation 2, is negligible and does not proceed in any direction (Stolper and Eiler, 2015). Under most natural conditions, the apparent equilibrium blocking temperature for magnesite is at least ~490 °C as recorded by the magnesite (Isua, Greenland) (Table 2), which is higher than calcite by ~300 to 350 °C (blocking temperature of calcite: ~150-200 °C; Dennis and Schrag, 2010) and dolomite by at least ~200°C (blocking temperature of dolomite ranges between 260 and 350 °C (Ferry *et al*., 2011; Vandeginste *et al*., 2014). It follows that the dolomite coexisting with magnesite (Isua, Greenland) records a temperature of 326 °C, which lies within the range of apparent blocking temperatures of dolomite. Additionally, dolomite (Ludlow, Vermont) has a Δ_{47} composition that corresponds to a clumped-isotope temperature of 360 °C (Table 2, Fig. 9b), which is below the expected mineralization temperature for the talc-magnesite-dolomite system (*cf*. Table 1; Section 2.4.2), but is within error of the range of proposed blocking temperatures for dolomite (260-350 °C).

We thus suggest that magnesite preserves higher clumped-isotope temperatures than both calcite and dolomite, and can function as a clumped-isotope carbonate geothermometer with a broader temperature application range. We assume that the Greenland magnesite-dolomite vein cooled faster than sedimentary and metamorphosed carbonates (*e.g*., marble) and thus preserves the original crystallization temperature of the metasomatic event, given that the apparent equilibrium blocking temperature is a function of cooling rate (Stolper and Eiler, 2015). The sampled magnesite+dolomite+talc vein appears to have formed as a single-stage fracture and does not present a reaction aureole or folding, which may be indicative of secondary resetting by subsequent heating. This possibility allows us to assume that the vein was not affected by post-mineralization isotopic re-ordering due to thermal changes (*e.g.*, Henkes *et al*., 2013). However, temperature limits based on clumped-isotope compositions in magnesite need to be further evaluated in regard to solid-state reordering (*e.g.*, Henkes *et al*., 2014) and explored in other geologic settings where high temperature magnesite occurs and cooling rates can be better approximated (*e.g.*, sedimentary and diagenetic magnesite).

6. Implications for carbon capture and storage in ultramafic rocks

Natural occurrences of magnesium carbonates from a broad range of geologic environments provide fundamental constraints on carbon capture and storage (CCS) in ultramafic rocks. The study of these natural analogues, such as those presented here, complements the array of research methodologies directly applied to CCS, which include laboratory experiments (*e.g.*, Olsson *et al*., 2012; Johnson *et al*., 2014; Harrison *et al*., 2015), geochemical and fracture modeling (*e.g.*, Rudge *et al*., 2010; Klein and Garrido, 2011; Bea *et al*., 2012; Paukert *et al.*, 2012), and pilot and proposed injections of CO_2, such as the CarbFix project in Iceland basalts (Matter *et al*., 2009; Gislason *et al*., 2010; Matter *et al*., 2011; Gislason and Oelkers, 2014) and in the Samail ophiolite in Oman (Kelemen *et al*., 2013). Our results for cryptocrystalline magnesite from some of the largest deposits in the world indicate that Δ_{47} compositions are surprisingly uniform. The similar clumped-isotope temperatures, combined with calculated $\delta^{18}O_{fluid}$ and $\delta^{13}C_{CO2}$ values, suggest that circulating meteoric waters played an important role in the genesis of the deposits. Likewise, preserved Δ_{47} compositions and clumped-isotope temperatures record ambient conditions in the formation of hydrous magnesium carbonates in ultramafic rocks, indicating that direct uptake of CO_2 occurs readily at surface conditions. These natural examples demonstrate that magnesium carbonate mineralization could be replicated in engineered CO_2 reactions in ultramafic rocks at the surface and shallow depths, although the slow kinetics of such engineered reactions may render this approach impractical (Johnson *et al*., 2014). Collectively, our results support the application of clumped-isotope thermometry to guide the possible implementation of engineered carbonation in ultramafic rocks and other lithologies.

7. Conclusions

Our study demonstrates the application of carbonate clumped-isotope thermometry in addressing the formation of a wide variety of magnesium carbonates in ultramafic rocks. The broad range of samples presented here enables the study of portions of the shallow crust where CO_2-bearing fluids mediate the formation of cryptocrystalline magnesite ore deposits, surface hydrous magnesium carbonates, and hydrothermal/metamorphic carbonates and related talc ores. Determining the preserved compositions of Δ_{47} compositions and corresponding clumped-isotope temperature of cryptocrystalline magnesite provides a new framework for revisiting the paragenesis of similar deposits worldwide (*e.g.* Fig. 10). We show that hydrous magnesium carbonates formed at the surface in sheared serpentinized-peridotite rocks preserve clumped-isotope temperatures consistent with average historical ambient temperatures, demonstrating the importance of seasonality in the formation of hydromagnesite and artinite in the California Coast Ranges. Likewise, clumped-isotope thermometry can be applied to high-temperature magnesite and dolomite, where results are broadly consistent with thermodynamic and independent constraints, despite expected potential effects of isotopic solid state re-ordering. Because of the more elevated apparent equilibrium blocking temperature of magnesite relative to calcite and dolomite, magnesite can be used to establish a broader magnesite geothermometer, and improve elemental solvus thermometry of the carbonate systems, including those containing calcite and dolomite

(*e.g.*, Sheppard and Schwarcz, 1970). Magnesium carbonates hosted in ultramafic rocks represent an important example of multiple processes that convert CO_2 from fluid to solid phase, a transformation that can be traced using carbonate clumped-isotope thermometry.

8. Acknowledgments

We thank the Global Climate and Energy Project (GCEP) at Stanford University for funding and continued support (Award GCEP-48942 to K. Maher, D.K. Bird and G.E. Brown, Jr.), the School of Earth Sciences Diversity Incentive Fund fellowship and the McGee Levorsen Grant to P. García del Real. Clumped-isotope measurements were performed using instruments from the Qatar Carbonates and Carbonate Storage Research Centre (QCCSRC) at Imperial College London, financed by Qatar Petroleum, Shell, and the Qatar Science and Technology Park (QSTP). We would also like to specially thank T. Benson, A. Dale, S. Davis, R. Gould, A. Harrison, D. E. Ibarra, N. Johnson, J. MacDonald, H. Mirnejad, J. Nelson, C. Stranzl (RHI AG Company), N. Sullivan, D. Thomas, T. Unterweissacher, and V. Vandeginste for enriching discussions and suggestions, furnishing samples, and invaluable field support. We also acknowledge three anonymous reviewers whose comments improved this manuscript.

9. Figure Captions

Figure 1. A. Location map of cryptocrystalline magnesite districts hosted in ultramafic rocks and high-temperature magnesium carbonates. Additional sample information is provided in Table 1. **B.** Distribution of ultramafic bodies in California and type of magnesium carbonate collected from each locality. Samples for this study are from three main areas: The McLaughlin serpentinite body in the Northern Coast Ranges; the Del Puerto ophiolite and related serpentinized peridotite; and New Idria serpentinite. Diamonds represent weather stations from which precipitation and temperature records have been used to constrain the formation of hydrous magnesium carbonates. From north to south: Blank diamonds correspond to stations in the vicinity of McLaughlin: (1) Clearlake 4 SE, (2) Middletown, and (3) Calistoga. Filled diamonds represent stations near Red Mountain and the Del Puerto roadcut hydromagnesite deposit: (4) Mount Hamilton, (5) Gerber Ranch, (6) Del Puerto Road Camp, and (7) Diablo Grande. Semi-filled diamonds near New Idria indicate stations (8) Panoche 2-W, (9) Idria and (10) Pinnacles National Monument. Exact location and distance to sampling site are shown in Table A3.

Figure 2. **A**. SEM photograph of Red Mountain magnesite fragments loaded on a petrographic slide, which allows to show a 3D texture of the cryptonodules that dominate the magnesite mineralization and discrete larger magnesite crystals. Note the high porosity of cryptocrystalline magnesite. **B.** Detail of magnesite crystals within nodular crystalline magnesite. **C.** SEM photograph of Red Mountain cryptocrystalline magnesite from a thin section. Photograph shows the interior of a magnesite crystal in a matrix of homogenous cryptonodular crystals of magnesite **D**. SEM photograph of hydromagnesite and dypinguite from the mine adit of Red Mountain. Rose blades represent hydromagnesite and dypingite exhibits a fibrous habit. **E**. and **F**. SEM image detail of

hydromagnesite blades from the Red Mountain crustiform carbonates.

Figure 3. Examples of cryptocrystalline magnesite from Red Mountain, California (USA). **A**. Massive magnesite vein at Red Mountain, thickness ~20m and several hundred meters in horizontal and lateral extent. Note sharp contacts with peridotite and secondary amorphous silica slickenside. **B**. Stockwork magnesite. **C.** Magnesite nodule at Red Mountain within a serpentine and peridotite matrix.

Figure 4. Hydrous magnesium carbonates from surface exposures (California Coast Ranges). **A.** Hydromagnesite veinlets, nodules, and coalesced nodules from an exposed transect of massively sheared and friable serpentinite at the McLaughlin Reserve, California. Notice distance from soil horizon and vegetation. Unreplaced blocks of peridotite-serpentinite on the lower right corner of photograph. **B**. Hydromagnesite spherical concretions embedded in serpentinite. If removed, the hydromagnesite nodules leave a void round cavity. **C.** Hydromagnesite nodules and veinlets exposed along a roadcut (Del Puerto Road) through the peridotite segment of the Del Puerto ophiolite, California. Lower right section of photograph shows where the road begins. Note the progression from fresh, unmineralized peridotite to shear serpentinite to hydrmagnesite mineralization. **D.** Detail of mineralization at Del Puerto road. **E.** Hydromagnesite nodules in sheared serpentinite of New Idria, California. **F**. Artinite crystals growing on serpentinite surfaces in mine tailings of New Idria, California. (Photo credit for A and B: D.E. Ibarra)

Figure 5. Crustiform, hydrous magnesium carbonates from Red Mountain mine adit. **A**. Map of level 3040 ft. (927 m) at Red Mountain showing the location of the carbonate coatings and the temperature gradient prevalent at the mine. Temperature at the collection site is constant at 11.3°C. Temperatures in sections ~>150 m from the adit entrance are consistently 11.3±0.1°C regardless of time of the day. Temperature decreases from 14.0°C at 1 m from entrance to 12.2°C at 90 m, and at ~150 m the temperature reaches a constant temperature of 11.3°C. Other sections of the mine at different levels exhibit temperatures of 11.3±0.1°C, which suggest that our temperature estimate for prevalent temperatures in the mine does not vary. **B.** Photograph showing the layered white admixture of hydromagnesite and minor dypingite, and the nearly transparent nesquehonite that develops at the end of the carbonate envelope. **C**. Photograph highlighting the formation of nesquehonite over the hydromagnesite-dypingite crust and the droplet-like nesquehonite. **D.** Cross-section detail of the interface between ultramafic rock contact and crustiform hydrous magnesium carbonates. The carbonate preserves a thin layer of ultramafic dust probably derived from mining operations. Hydromagnesite and dypingite develop along the contact wall, differentiated by the creamy and white color, and nodular habit. Nesquehonite develops at sharp contact with the hydromagnesite-dypingite as the final stage of the mineralization and displays transparent, salt-like bladed crystals.

Figure 6. Magnesite-dolomite vein mineralization in ultramafic exposures in Isua, Greenland, and sample example of dolomite from Vermont. **A**. Talc-magnesite-dolomite vein, thickness ~30 cm and several tens of meters in lateral extent. Vein cuts through

>3715 Ma schistose and altered undifferentiated ultramafic rock, which includes metasomatised dunites and layered peridotite (Nutman and Friend, 2009; Pope *et al*., 2012; Szilas *et al*., 2015). **B**. Detail of coeval magnesite-dolomite mineralization in equilibrium with talc. Magnesite is readily identified by the reddish color, whereas dolomite exhibits a white tone. **C.** Dolomite crystal from Ludlow, Vermont.

Figure 7. Synthetic magnesite and hydromagnesite**. A.** SEM photograph of olivine-magnesite from experiments reported in Johnson *et al.* (2014). Note the spiral growth of magnesite crystals on olivine surfaces. **B**. SEM photograph of the synthetic hydromagnesite (Sample Mg-3) precipitated at 80°C following the methods of Kluge and John (2015).

Figure 8. Samples of known temperature used to evaluate the acid fractionation correction. Acid-corrected Δ_{47} values of experimental magnesite (black circles) and hydromagnesite (filled triangles) samples in the CDES scale of Dennis *et al*. (2011) and the magnesite samples (white circles) from Falk and Kelemen (2015). We apply an acid correction of +0.069 ‰, consistent with the fractionation for various carbonates, which leads to a Δ_{47}-T relationship of magnesite and hydromagnesite that follows the same calibration line as for calcite. The polynomial fit of Falk and Kelemen (2015) is shown for comparison.

Figure 9. Acid-corrected Δ_{47} values and clumped-isotope temperatures of natural magnesium carbonate samples. Also shown is the calibration line of Kluge *et al*. 2015 (Equation 4) employed to determine clumped temperatures. **A.** Δ_{47} values and clumped-isotope temperatures (acid corrected to +0.069 ‰) of cryptocrystalline magnesite (circles; Red Mountain, CA (USA), Austria, Turkey and Iran); California Coast Ranges surface hydrous magnesium carbonates (squares; McLaughlin, Del Puerto, New Idria); and Red Mountain mine adit carbonates (triangles). Independent temperature for Red Mountain mine adit samples (hydromagnesite and nesquehonite) is the temperature of the mine (11.3°C). **B.** Δ_{47} values and clumped-isotope temperatures (acid corrected to +0.069 ‰) of high-temperature magnesite and dolomite from Isua, Greenland and Vermont.

Figure 10. Oxygen and carbon isotope compositions of magnesium carbonates and corresponding mineralizing fluid (water and CO_2). **A.** Measured values of oxygen and carbon isotope compositions (Table 2) of: cryptocrystalline magnesite from this study (Red Mountain, California, USA, Austria, Turkey and Iran; filled circles); worldwide compilation of other cryptocrystalline magnesite deposits (data and references in Table A1 and A4; gray field); hydrous magnesium carbonates (California Coast Ranges; brown squares); mine adit carbonates (Red Mountain, California, USA; yellow triangles); and high-temperature carbonates (Vermont; red rhomb and Greenland; orange rhomb). **B.** Corresponding oxygen isotope composition of mineralizing solutions and carbon isotope composition of mineralizing CO_2 (Table 3). Box areas represent fields of average oxygen isotope compositions of natural waters (Data in Table A5). Lower boxes represent global ranges of carbon isotope compositions of CO_2 reservoirs relevant to our discussion (Data in Table A5).

Figure 11. Geologic or experimental (known temperature in °C) versus clumped-isotope temperature (in °C). Data for geologic temperature estimates for cryptocrystalline magnesite are given in Table A1. Error bars represent standard error between minimum and maximum estimated temperatures for each location (Table A1). Data for geologic temperature estimates for hydrous magnesium carbonates (California Coast Ranges) are taken from Figs. A4 and A5. Errors bars represent standard error between minimum and maximum temperatures recorded at weather stations (Table A3). The diagonal 1:1 line represents the correlation between expected geologic or experimental temperatures in relation to clumped-isotope temperature. Also shown: the hydrous magnesium carbonates (yellow triangles) from the Red Mountain mine adit expected to have formed at 11.3 °C; olivine-magnesite experiments (white triangles) at 60 °C and hydromagnesite experiments at 80 °C (blue triangles). The arrows represent the deviation from expected temperature for Red Mountain mine adit (nesquehonite, sample *DPT12-10 Salt*) (Section 5.4) and for synthetic magnesite from olivine dissolution experiments (samples *0209* and *1210P*) (Section 5.1).

10. References

Abu-Jaber N. S. and Kimberley M. M. (1992a) Origin of ultramafic-hosted magnesite on Margarita Island, Venezuela. *Miner. Depos.* **27**, 234–241.

Abu-Jaber N. S. and Kimberley M. M. (1992b) Origin of ultramafic-hosted vein magnesite deposits. *Ore Geol. Rev.* **7**, 155–191.

Affek H. P., Bar-Matthews M., Ayalon A., Matthews A. and Eiler J. M. (2008) Glacial/interglacial temperature variations in Soreq cave speleothems as recorded by "clumped isotope" thermometry. *Geochim. Cosmochim. Acta* **72**, 5351–5360.

Affek H. P. and Eiler J. M. (2006) Abundance of mass $^{47}CO_2$ in urban air, car exhaust, and human breath. *Geochim. Cosmochim. Acta* **70**, 1–12.

Affek H. P., Matthews A., Ayalon A., Bar-Matthews M., Burstyn Y., Zaarur S. and Zilberman T. (2014) Accounting for kinetic isotope effects in Soreq Cave (Israel) speleothems. *Geochim. Cosmochim. Acta* **143**, 303–318.

Affek H. P. and Zaarur S. (2014) Kinetic isotope effect in CO_2 degassing: Insight from clumped and oxygen isotopes in laboratory precipitation experiments. *Geochim. Cosmochim. Acta* **143**, 319–330.

Aharon P. (1988) A stable-isotope study of magnesites from the Rum Jungle Uranium Field, Australia: Implications for the origin of strata-bound massive magnesites. *Chem. Geol.* **69**, 127–145.

Armstrong T. R. and Tracy R. J. (2000) One-dimensional thermal modelling of Acadian metamorphism in southern Vermont, USA. *J. Metamorph. Geol.* **18**, 625–638.

Barnes I. and O'Neil J. R. (1969) The Relationship between Fluids in Some Fresh Alpine-Type Ultramafics and Possible Modern Serpentinization, Western United States. *Geol. Soc. Am. Bull.* **80**, 1947–1960.

Barnes I., O'Neill J. R., Rapp J. B. and White D. E. (1973) Silica-Carbonate Alteration of Serpentine: Wall Rock Alteration in Mercury Deposits of the California Coast Ranges. *Econ. Geol.* **68**, 388–398.

Bea S., Wilson S., Mayer K., Dipple G., Power I. and Gamazo P. (2012) Reactive Transport Modeling of Natural Carbon Sequestration in Ultramafic Mine Tailings.

Vadose Zo. J. **11**, 0.
Beinlich A. and Austrheim H. (2012) In situ sequestration of atmospheric CO_2 at low temperature and surface cracking of serpentinized peridotite in mine shafts. *Chem. Geol.* **332-333**, 32–44.
Bénézeth P., Ménez B. and Noiriel C. (2009) CO_2 geological storage: Integrating geochemical, hydrodynamical, mechanical and biological processes from the pore to the reservoir scale. *Chem. Geol.* **265**, 1–2.
Bénézeth P., Saldi G. D., Dandurand J.-L. and Schott J. (2011) Experimental determination of the solubility product of magnesite at 50 to 200°C. *Chem. Geol.* **286**, 21–31.
Blank J. G., Green S. J., Blake D., Valley J. W., Kita N. T., Treiman A. and Dobson P. F. (2009) An alkaline spring system within the Del Puerto Ophiolite (California, USA): A Mars analog site. *Planet. Space Sci.* **57**, 533–540.
Bodenlos A. J. (1950) Geology of the Red Mountain Magnesite District, Santa Clara and Stanislaus Counties, California. *Calif. J. Mines Geol.* **46**, 223–278.
Boschi C., Dini A., Dallai L., Ruggieri G. and Gianelli G. (2009) Enhanced CO_2-mineral sequestration by cyclic hydraulic fracturing and Si-rich fluid infiltration into serpentinites at Malentrata (Tuscany, Italy). *Chem. Geol.* **265**, 209–226.
Braithwaite C. J. R. and Zedef V. (1996) Hydromagnesite stromatolites and sediments in an alkaline lake, Salda Golu, Turkey. *J. Sediment. Res.* **66**, 991–1002.
Breecker D. O., Sharp Z. D. and McFadden L. D. (2009) Seasonal bias in the formation and stable isotopic composition of pedogenic carbonate in modern soils from central New Mexico, USA. *Geol. Soc. Am. Bull.* **121** , 630–640.
Brinker C. J. and Scherer G. W. (1990) *Sol-gel science: the physics and chemistry of sol-gel processing*, Academic Press, Inc., San Diego, CA.
Bristol C. C. (1972) Quantitative Determination of some Carbonate Minerals in Greenschist Facies Meta-volcanic Rocks. *Can. J. Earth Sci.* **9**, 36–42.
Bristow T. F., Bonifacie M., Derkowski A., Eiler J. M. and Grotzinger J. P. (2011) A hydrothermal origin for isotopically anomalous cap dolostone cements from south China. *Nature* **474**, 68–71.
Bucher K. and Grapes R. (2011) Metamorphism of Ultramafic Rocks. In *Petrogenesis of Metamorphic Rocks* Springer Berlin Heidelberg. pp. 191–224.
Buhmann D. and Dreybrodt W. (1985) The kinetics of calcite dissolution and precipitation in geologically relevant situations of karst areas. *Chem. Geol.* **48**, 189–211.
Cañaveras J. C., Hoyos M., Sanchez-Moral S., Sanz-Rubio E., Bedoya J., Soler V., Groth I., Schumann P., Laiz L., Gonzalez I. and Saiz-Jimenez C. (1999) Microbial Communities Associated With Hydromagnesite and Needle-Fiber Aragonite Deposits in a Karstic Cave (Altamira, Northern Spain). *Geomicrobiol. J.* **16**, 9–25.
Carreira P. M., Marques J. M., Graça R. C. and Aires-Barros L. (2008) Radiocarbon application in dating "complex" hot and cold CO_2-rich mineral water systems: A review of case studies ascribed to the northern Portugal. *Appl. Geochemistry* **23**, 2817–2828.
Chacko T. and Deines P. (2008) Theoretical calculation of oxygen isotope fractionation factors in carbonate systems. *Geochim. Cosmochim. Acta* **72**, 3642–3660.
Cisneros S. L., Witkowski R. E. and Oswald D. L. (1977) Artinite from San Benito

Country, California. *Mineral. Rec.*, 457–460.
Daëron M., Guo W., Eiler J., Genty D., Blamart D., Boch R., Drysdale R., Maire R., Wainer K. and Zanchetta G. (2011) $^{13}C^{18}O$ clumping in speleothems: Observations from natural caves and precipitation experiments. *Geochim. Cosmochim. Acta* **75**, 3303–3317.
Dale A., John C. M., Mozley P. S., Smalley P. C. and Muggeridge A. H. (2014) Time-capsule concretions: Unlocking burial diagenetic processes in the Mancos Shale using carbonate clumped isotopes. *Earth Planet. Sci. Lett.* **394**, 30–37.
Dandurand J. L. and Schott J. (1975) Sur la stabilité des carbonates naturels. Valeurs nouvelles des enthalpies libres de formation des phases des systèmes $MgO\text{-}CO_2\text{-}H_2O$ et $CaO\text{-}MgO\text{-}CO_2\text{-}H_2O$. *Comptes rendues Hebd. des Seances l'Academie des Sci. Série C Sci. Chim.* **280**, 1247–1250.
Deelman J. C. (1999) Low-temperature nucleation of magnesite and dolomite. *Neues Jahrb. Fur Mineral. Monatshefte* **7**, 289–302.
Defliese W. F., Hren M. T. and Lohmann K. C. (2015) Compositional and temperature effects of phosphoric acid fractionation on Δ_{47} analysis and implications for discrepant calibrations. *Chem. Geol.* **396**, 51–60.
Dennis K. J., Affek H. P., Passey B. H., Schrag D. P. and Eiler J. M. (2011) Defining an absolute reference frame for "clumped" isotope studies of CO_2. *Geochim. Cosmochim. Acta* **75**, 7117–7131.
Dennis K. J. and Schrag D. P. (2010) Clumped isotope thermometry of carbonatites as an indicator of diagenetic alteration. *Geochim. Cosmochim. Acta* **74**, 4110–4122.
Dreybrodt W. (1999) Chemical kinetics, speleothem growth and climate. *Boreas* **28**, 347–356.
Dymek R. F., Brothers S. C. and Schiffries C. M. (1988) Petrogenesis of ultramafic metamorphic rocks from the 3800 MA Isua supracrustal belt, West Greenland. *J. Petrol.* **29**, 1353–1397.
Eagle R. A, Tütken T., Martin T. S., Tripati A. K., Fricke H. C., Connely M., Cifelli R. L. and Eiler J. M. (2011) Dinosaur body temperatures determined from isotopic (^{13}C-^{18}O) ordering in fossil biominerals. *Science* **333**, 443–5.
Ece Ö. I., Matsubaya O. and Çoban F. (2005) Genesis of hydrothermal stockwork-type magnesite deposits associated with ophiolite complexes in the Kütahya-Eskişehir region, Turkey. *Neues Jahrb. für Mineral. - Abhandlungen* **181**, 191–205.
Eiler J. M. (2007) "Clumped-isotope" geochemistry—The study of naturally-occurring, multiply-substituted isotopologues. *Earth Planet. Sci. Lett.* **262**, 309–327.
Eiler J. M. (2011) Paleoclimate reconstruction using carbonate clumped isotope thermometry. *Quat. Sci. Rev.* **30**, 3575–3588.
Eiler J. M., Bergquist B., Bourg I., Cartigny P., Farquhar J., Gagnon A., Guo W., Halevy I., Hofmann A., Larson T. E., Levin N., Schauble E. A. and Stolper D. (2014) Frontiers of stable isotope geoscience. *Chem. Geol.* **372**, 119–143.
Eiler J. M. and Schauble E. (2004) $^{18}O^{13}C^{16}O$ in Earth's atmosphere. *Geochim. Cosmochim. Acta* **68**, 4767–4777.
Evans B. W. (2010) Lizardite versus antigorite serpentinite: Magnetite, hydrogen, and life(?). *Geology* **38**, 879–882.
Falk E. S. and Kelemen P. B. (2015) Geochemistry and petrology of listvenite in the Samail ophiolite, Sultanate of Oman: Complete carbonation of peridotite during

ophiolite emplacement. *Geochim. Cosmochim. Acta* **160**, 70–90.
Fallick A. E., Ilich M. and Russell M. J. (1991) A stable isotope study of the magnesite deposits associated with the alpine-type ultramafic rocks of Yugoslavia. *Econ. Geol.* **86**, 847–861.
Fantle M. S., Maher K. M. and DePaolo D. J. (2010) Isotopic approaches for quantifying the rates of marine burial diagenesis. *Rev. Geophys.* **48**, 1–38.
Faure G. and Mensing T. M. (2005) *Isotopes: principles and applications*., John Wiley & Sons Inc. Hoboken, NJ. 897 p.
Fernandez A., Tang J. and Rosenheim B. E. (2014) Siderite "clumped" isotope thermometry: A new paleoclimate proxy for humid continental environments. *Geochim. Cosmochim. Acta* **126**, 411–421.
Ferry J. M., Passey B. H., Vasconcelos C. and Eiler J. M. (2011) Formation of dolomite at 40-80°C in the Latemar carbonate buildup, Dolomites, Italy, from clumped isotope thermometry. *Geology* **39**, 571–574.
Fuex A. and Baker D. R. (1973) Stable carbon isotopes in selected granitic, mafic, and ultramafic igneous rocks. *Geochim. Cosmochim. Acta*.
Gartzos E. (2004) Comparative stable isotopes study of the magnesite deposits of Greece. *Bull. Geol. Soc. Greece. Proc. 10th Int. Congr.* **XXXVI**, 196–203.
Genth F. A. and Penfield S. L. (1890) On Lansfordite, nesquehonite, a new mineral, and pseudomorphs of nesquehonite after lansfordite. *Am. J. Sci.* **Series 3 V**, 121–137.
Ghoneim M. F., Saleem I. A. and Hamdy M. M. (2003) Origin of magnesite veins in serpentinites from Mount El-Rubshi and Mount El-Maiyit, Eastern Desert Egypt. *Arch. Mineral.* **2002**, 41–63.
Ghosh P., Adkins J., Affek H., Balta B., Guo W., Schauble E. A., Schrag D. and Eiler J. M. (2006) ^{13}C–^{18}O bonds in carbonate minerals: A new kind of paleothermometer. *Geochim. Cosmochim. Acta* **70**, 1439–1456.
Gislason S. R. and Oelkers E. H. (2014) Carbon storage in basalt. *Science (80).* **344**, 373–4.
Gislason S. R., Wolff-Boenisch D., Stefansson A., Oelkers E. H., Gunnlaugsson E., Sigurdardottir H., Sigfusson B., Broecker W. S., Matter J. M. and Stute M. (2010) Mineral sequestration of carbon dioxide in basalt: A pre-injection overview of the CarbFix project. *Int. J. Greenh. Gas Control* **4**, 537–545.
Golyshev S. I., Padalko N. L. and Pechenkin S. A. (1981) Fractiontation of stable oxygen and carbon isotopes in carbonate systems. *Geochemistry Int.* **18**, 85–99.
Guo W., Mosenfelder J. L., Goddard W. A. and Eiler J. M. (2009) Isotopic fractionations associated with phosphoric acid digestion of carbonate minerals: Insights from first-principles theoretical modeling and clumped isotope measurements. *Geochim. Cosmochim. Acta* **73**, 7203–7225.
Hänchen M., Prigiobbe V., Baciocchi R. and Mazzotti M. (2008) Precipitation in the Mg-carbonate system—effects of temperature and CO_2 pressure. *Chem. Eng. Sci.* **63**, 1012–1028.
Hansen L. D., Dipple G. M., Gordon T. M. and Kellett D. A. (2005) Carbonated Serpentinite (Listwanite) At Atlin, British Columbia: a Geological Analogue To Carbon Dioxide Sequestration. *Can. Mineral.* **43**, 225–239.
Harrison A. L., Dipple G. M., Power I. M. and Mayer K. U. (2015) Influence of surface passivation and water content on mineral carbonation rates: Implications for CO_2

sequestration in mine tailings. *Geochim. Cosmochim. Acta* **148**, 477–495.
Harrison A. L., Power I. M. and Dipple G. M. (2013) Accelerated carbonation of brucite in mine tailings for carbon sequestration. *Environ. Sci. Technol.* **47**, 126–134.
Harrison S., Safford H. D., Grace J. B., Viers J. H. and Davies K. F. (2006) Regional and local species richness in an insular environment: Serpentine plants in California. *Ecol. Monogr.* **76**, 41–56.
Hazen R. M. and Schiffries C. M. (2013) Why Deep Carbon? *Rev. Mineral. Geochemistry* **75**, 1–6.
Henkes G. A., Passey B. H., Grossman E. L., Shenton B. J., Pérez-Huerta A. and Yancey T. E. (2014) Temperature limits for preservation of primary calcite clumped isotope paleotemperatures. *Geochim. Cosmochim. Acta* **139**, 362–382.
Henkes G. A., Passey B. H., Wanamaker A. D., Grossman E. L., Ambrose W. G. and Carroll M. L. (2013) Carbonate clumped isotope compositions of modern marine mollusk and brachiopod shells. *Geochim. Cosmochim. Acta* **106**, 307–325.
Hill P. S., Tripati A. K. and Schauble E. A. (2014) Theoretical constraints on the effects of pH, salinity, and temperature on clumped isotope signatures of dissolved inorganic carbon species and precipitating carbonate minerals. *Geochim. Cosmochim. Acta* **125**, 610–652.
Horkel K., Ebner F. and Spötl C. (2009) Stable isotopic composition of cryptocrystalline magnesite from deposits in Turkey and Austria. *Geophys. Res. Abstr.* **11**.
Huntington K. W. and Lechler A. R. (2015) Carbonate clumped isotope thermometry in continental tectonics. *Tectonophysics* **647-648**, 1–20.
Huntington K. W., Eiler J. M., Affek H. P., Guo W., Bonifacie M., Yeung L. Y., Thiagarajan N., Passey B., Tripati A., Daëron M. and Came R. (2009) Methods and limitations of "clumped" CO_2 isotope (Δ_{47}) analysis by gas-source isotope ratiomass spectrometry. *J. Mass Spectrom.* **44**, 1318–1329.
IAEA/WMO (2015) Global Network of Isotopes in Precipitation. *The GNIP Database*. Accessible at: http://www.iaea.org/water
Isshiki M., Irifune T., Hirose K., Ono S., Ohishi Y., Watanuki T., Nishibori E., Takata M. and Sakata M. (2004) Stability of magnesite and its high-pressure form in the lowermost mantle. *Nature* **427**, 60–63.
Jedrysek M. O. and Halas S. (1990) The origin of magnesite deposits from the Polish Foresudetic Block ophiolites: preliminary $\delta^{13}C$ and $\delta^{18}O$ investigations. *Terra Nov.* **2**, 154–159.
Johnson N. C., Thomas B., Maher K., Rosenbauer R. J., Bird D. and Brown G. E. (2014) Olivine dissolution and carbonation under conditions relevant for in situ carbon storage. *Chem. Geol.* **373**, 93–105.
Jurković I., Palinkaš L. A., Garašić V. and Palinkaš S. S. (2012) Genesis of vein-stockwork cryptocrystalline magnesite from the Dinaride ophiolites. *Ofioliti* **37**, 13–26.
Kahya A. and Kuşcu M. (2014) Source of the mineralizing fluids in ultramafic related magnesite in the Eskişehir area, northwest Turkey, along the İzmir-Ankara suture: A stable isotope study. *Turkish J. Earth Sci.* **23**, 1–15.
Kauffman E. (2003) Atlas of the biodiversity of California: climate and topography. 12–15. *California Department of Fish and Game*.
Kele S., Breitenbach S. F. M., Capezzuoli E., Meckler A. N., Ziegler M., Millan I. M.,

Kluge T., Deák J., Hanselmann K., John C. M., Yan H., Liu Z. and Bernasconi S. M. (2015) Temperature dependence of oxygen- and clumped isotope fractionation in carbonates: a study of travertines and tufas in the 6-95°C temperature range. *Geochim. Cosmochim. Acta* **168**, 172–192.

Kelemen P. B. and Matter J. (2008) In situ carbonation of peridotite for CO_2 storage. *Proc. Natl. Acad. Sci.* **105**, 17295–17300.

Kelemen P. B., Matter J., Streit E. E., Rudge J. F., Curry W. B. and Blusztajn J. (2011) Rates and Mechanisms of Mineral Carbonation in Peridotite: Natural Processes and Recipes for Enhanced, in situ CO_2 Capture and Storage. *Annu. Rev. Earth Planet. Sci.* **39**, 545–576.

Kelemen P., Rajhi A. Al, Godard M., Ildefonse B., Köpke J., MacLeod C., Manning C., Michibayashi K., Nasir S., Shock E., Takazawa E. and Teagle D. (2013) Scientific Drilling and Related Research in the Samail Ophiolite, Sultanate of Oman. *Sci. Drill.*, 64–71.

Kendall C. and Coplen T. B. (2001) Distribution of oxygen-18 and deuterium in river waters across the United States. *Hydrol. Process.* **15**, 1363–1393.

Kesseli J. (1942) The Climates of California According to the Köppen Classification. *Geogr. Rev.* **32**, 476–480.

Kim S.-T. and O'Neil J. R. (1997) Equilibrium and nonequilibrium oxygen isotope effects in synthetic carbonates. *Geochim. Cosmochim. Acta* **61**, 3461–3475.

Klein F. and Garrido C. J. (2011) Thermodynamic constraints on mineral carbonation of serpentinized peridotite. *Lithos* **126**, 147–160.

Kluge T. and Affek H. P. (2012) Quantifying kinetic fractionation in Bunker Cave speleothems using Δ_{47}. *Quat. Sci. Rev.* **49**, 82–94.

Kluge T., Affek H. P., Marx T., Aeschbach-Hertig W., Riechelmann D. F. C., Scholz D., Riechelmann S., Immenhauser a., Richter D. K., Fohlmeister J., Wackerbarth a., Mangini A. and Spötl C. (2013) Reconstruction of drip-water $\delta^{18}O$ based on calcite oxygen and clumped isotopes of speleothems from Bunker Cave (Germany). *Clim. Past* **9**, 377–391.

Kluge T., Affek H. P., Zhang Y. G., Dublyansky Y., Spötl C., Immenhauser A. and Richter D. K. (2014) Clumped isotope thermometry of cryogenic cave carbonates. *Geochim. Cosmochim. Acta* **126**, 541–554.

Kluge T. and John C. M. (2015) Effects of brine chemistry and polymorphism on clumped isotopes revealed by laboratory precipitation of mono- and multiphase calcium carbonates. *Geochim. Cosmochim. Acta* **160**, 155–168.

Kluge T., John C. M., Jourdan A.-L., Davis S. and Crawshaw J. (2015) Laboratory calibration of the calcium carbonate clumped isotope thermometer in the 25–250°C temperature range. *Geochim. Cosmochim. Acta* **157**, 213–227.

Königsberger E., Königsberger L. C. and Gamsjäger H. (1999) Low-temperature thermodynamic model for the system Na_2CO_3-$MgCO_3$-$CaCO_3$-H_2O. *Geochim. Cosmochim. Acta* **63**, 3105–3119.

Kralik M., Aharon P., Schroll E. and Zachmann D. (1989) Carbon and oxygen isotope systematics of magnesites: a review. In *Magnesite. Geology, Mineralogy, Geochemistry, Formation of Mg-Carbonates* (ed. P. Moller). Monograph Series on Mineral Deposits 28 Gebruder Borntraeger, Berlin-Stuttgart. 197-223 pp.

Kruckeberg A. R. (1992) Plant life of western North American ultramafics. In *The*

Ecology of Areas with Serpentinized Rocks (eds. B. A. Roberts and J. Proctor). Geobotany. Springer Netherlands. pp. 31–73.

Lappin M. A. and Smith D. C. (1978) Mantle-equilibrated orthopyroxene eclogite pods from the basal gneisses in the selje district, Western Norway. *J. Petrol.* **19**, 530–584.

Leng M. J. and Marshall J. D. (2004) Palaeoclimate interpretation of stable isotope data from lake sediment archives. *Quat. Sci. Rev.* **23**, 811–831.

Lesko I. (1972) Uber die Bildung von Magnesidagerstatten. *Miner. Depos.* **7**, 61–72.

Loyd S. J., Corsetti F. A., Eiler J. M. and Tripati A. K. (2012) Determining the Diagenetic Conditions of Concretion Formation: Assessing Temperatures and Pore Waters Using Clumped Isotopes. *J. Sediment. Res.* **82** , 1006–1016.

Maher K., Steefel C. I., DePaolo D. J. and Viani B. E. (2006) The mineral dissolution rate conundrum: Insights from reactive transport modeling of U isotopes and pore fluid chemistry in marine sediments. *Geochim. Cosmochim. Acta* **70**, 337–363.

Matter J. M., Broecker W. S., Gislason S. R., Gunnlaugsson E., Oelkers E. H., Stute M., Sigurdardóttir H., Stefansson A., Alfreðsson H. A., Aradóttir E. S., Axelsson G., Sigfússon B. and Wolff-Boenisch D. (2011) The CarbFix Pilot Project–Storing carbon dioxide in basalt. *Energy Procedia* **4**, 5579–5585.

Matter J. M., Broecker W. S., Stute M., Gislason S. R., Oelkers E. H., Stefánsson A., Wolff-Boenisch D., Gunnlaugsson E., Axelsson G. and Björnsson G. (2009) Permanent Carbon Dioxide Storage into Basalt: The CarbFix Pilot Project, Iceland. *Energy Procedia* **1**, 3641–3646.

Matter J. M. and Kelemen P. B. (2009) Permanent storage of carbon dioxide in geological reservoirs by mineral carbonation. *Nat. Geosci.* **2**, 837–841.

Matthews A. and Katz A. (1977) Oxygen isotope fractionation during the dolomitization of calcium carbonate. *Geochim. Cosmochim. Acta* **41**, 1431–1438.

Mavromatis V., Bundeleva I. A., Shirokova L. S., Millo C., Pokrovsky O. S., Bénézeth P., Ader M. and Oelkers E. H. (2015) The continuous re-equilibration of carbon isotope compositions of hydrous Mg carbonates in the presence of cyanobacteria. *Chem. Geol.* **404**, 41–51.

Mavromatis V., Pearce C. R., Shirokova L. S., Bundeleva I. A., Pokrovsky O. S., Benezeth P. and Oelkers E. H. (2012) Magnesium isotope fractionation during hydrous magnesium carbonate precipitation with and without cyanobacteria. *Geochim. Cosmochim. Acta* **76**, 161–174.

McCrea J. M. (1950) On the Isotopic Chemistry of Carbonates and a Paleotemperature Scale. *J. Chem. Phys.* **18**, 849.

McGetchin T. R. and Besancon J. R. (1973) Carbonate inclusions in mantle-derived pyropes. *Earth Planet. Sci. Lett.* **18**, 408–410.

Meckler A. N., Ziegler M., Millán M. I., Breitenbach S. F. M. and Bernasconi S. M. (2014) Long-term performance of the Kiel carbonate device with a new correction scheme for clumped isotope measurements. *Rapid Commun. Mass Spectrom.* **28**, 1705–1715.

Melezhik V. A., Fallick A. E., Medvedev P. V. and Makarikhin V. V. (2001) Palaeoproterozoic magnesite: Lithological and isotopic evidence for playa/sabkha environments. *Sedimentology* **48**, 379–397.

Mirnejad H., Ebrahimi-Nasrabadi K., Lalonde A. E. and Taylor B. E. (2008) Mineralogy, Stable Isotope Geochemistry, and Paragenesis of Magnesite Deposits

From the Ophiolite Belt of Eastern Iran. *Econ. Geol.* **103**, 1703–1713.
Mix H. T., Mulch A., Kent-Corson M. L. and Chamberlain C. P. (2011) Cenozoic migration of topography in the North American Cordillera. *Geol.* **39** , 87–90.
Murray S. T., Arienzo M. M. and Swart P. K. (2016) Determining the Δ_{47} acid fractionation in dolomites. *Geochim. Cosmochim. Acta* **174**, 42–53.
Nutman A. P., Allaart J. H., Bridgwater D., Dimroth E. and Rosing M. (1984) Stratigraphic and geochemical evidence for the depositional environment of the early Archaean Isua Supracrustal Belt, Southern West Greenland. *Precambrian Res.* **25**, 365–396.
Nutman A. P. and Friend C. R. L. (2009) New 1:20,000 scale geological maps, synthesis and history of investigation of the Isua supracrustal belt and adjacent orthogneisses, southern West Greenland: A glimpse of Eoarchaean crust formation and orogeny. *Precambrian Res.* **172**, 189–211.
Nutman A. P., McGregor V. R., Friend C. R. L., Bennett V. C. and Kinny P. D. (1996) The Itsaq Gneiss Complex of southern West Greenland; the world's most extensive record of early crustal evolution (3900-3600 Ma). *Precambrian Res.* **78**, 1–39.
O'Neil J. R. and Barnes I. (1971) C^{13} and O^{18} compositions in some fresh-water carbonates associated with ultramafic rocks and serpentinites: western United States. *Geochim. Cosmochim. Acta* **35**, 687–697.
Olsson J., Bovet N., Makovicky E., Bechgaard K., Balogh Z. and Stipp S. L. S. (2012) Olivine reactivity with CO_2 and H_2O on a microscale: Implications for carbon sequestration. *Geochim. Cosmochim. Acta* **77**, 86–97.
Oskierski H. C., Bailey J. G., Kennedy E. M., Jacobsen G., Ashley P. M. and Dlugogorski B. Z. (2013) Formation of weathering-derived magnesite deposits in the New England Orogen, New South Wales, Australia: Implications from mineralogy, geochemistry and genesis of the Attunga magnesite deposit. *Miner. Depos.* **48**, 525–541.
Oskierski H. C., Dlugogorski B. Z. and Jacobsen G. (2013) Sequestration of atmospheric CO_2 in a weathering-derived, serpentinite-hosted magnesite deposit: ^{14}C tracing of carbon sources and age constraints for a refined genetic model. *Geochim. Cosmochim. Acta* **122**, 226–246.
Passey B. H. and Henkes G. A. (2012) Carbonate clumped isotope bond reordering and geospeedometry. *Earth Planet. Sci. Lett.* **351-352**, 223–236.
Paukert A. N., Matter J. M., Kelemen P. B., Shock E. L. and Havig J. R. (2012) Reaction path modeling of enhanced in situ CO_2 mineralization for carbon sequestration in the peridotite of the Samail Ophiolite, Sultanate of Oman. *Chem. Geol.* **330-331**, 86–100.
Perry E. C. J. and Ahmad S. N. (1977) Carbon isotope composition of graphite and carbonate minerals from 3.8-AE metamorphosed sediments, Isukasia, Greenland. *Earth Planet. Sci. Lett.* **36**, 280–284.
Petrizzo D. A., Young E. D. and Runnegar B. N. (2014) Implications of high-precision measurements of ^{13}C-^{18}O bond ordering in CO_2 for thermometry in modern bivalved mollusc shells. *Geochim. Cosmochim. Acta* **142**, 400–410.
Petrov V. P. (1980) Magnesite deposits of Serbia and their origin. *Int. Geol. Rev.* **22**, 497–510.
Poage M. A. and Chamberlain C. P. (2001) Empirical Relationships Between Elevation

and the Stable Isotope Composition of Precipitation and Surface Waters: Considerations for Studies of Paleoelevation Change. *Am. J. Sci.* **301**, 1–15.

Pohl W. (1989) Comparative Geology of Magnesite Deposits and Occurrences. In *Magnesite. Geology, Mineralogy, Geochemistry, Formation of Mg-Carbonates* (ed. P. Moller). Monograph Series on Mineral Deposits 28. Gebruder Borntraeger, Berlin-Stuttgart. pp. 1–13.

Pohl W. (1990) Genesis of magnesite deposits - models and trends. *Geol. Rundschau* **79/2**, 291–299.

Pope E. C., Bird D. K. and Rosing M. T. (2012) Isotope composition and volume of Earth's early oceans. *Proc. Natl. Acad. Sci. U. S. A.* **109**, 4371–6.

Power I. M., Harrison A. L., Dipple G. M., Wilson S. A., Kelemen P. B., Hitch M. and Southam G. (2013a) Carbon Mineralization: From Natural Analogues to Engineered Systems. *Rev. Mineral. Geochemistry* **77**, 305–360.

Power I. M., Wilson S. A. and Dipple G. M. (2013b) Serpentinite Carbonation for CO_2 Sequestration. *Elements* **9**, 115–121.

Power I. M., Wilson S. A., Harrison A. L., Dipple G. M., Mccutcheon J., Southam G. and Kenward P. A. (2014) A depositional model for hydromagnesite-magnesite playas near Atlin, British Columbia, Canada. *Sedimentology*, 1701–1733.

Power I. M., Wilson S. A., Thom J. M., Dipple G. M., Gabites J. E. and Southam G. (2009) The hydromagnesite playas of Atlin, British Columbia, Canada: A biogeochemical model for CO_2 sequestration. *Chem. Geol.* **260**, 302–316.

Pronost J., Beaudoin G., Lemieux J.-M., Hébert R., Constantin M., Marcouiller S., Klein M., Duchesne J., Molson J. W., Larachi F. and Maldague X. (2012) CO_2-depleted warm air venting from chrysotile milling waste (Thetford Mines, Canada): Evidence for in-situ carbon capture from the atmosphere. *Geol.* **40** , 275–278.

Quade J., Eiler J., Daëron M. and Achyuthan H. (2013) The clumped isotope geothermometer in soil and paleosol carbonate. *Geochim. Cosmochim. Acta* **105**, 92–107.

Quesnel B., Boulvais P., Gautier P., Cathelineau M., John C. M., Dierick M., Agrinier P. and Drouillet M. (2016) Paired stable isotopes (O, C) and clumped isotope thermometry of magnesite and silica veins in the New Caledonia Peridotite Nappe. *Geochim. Cosmochim. Acta* **183**, 234–249.

Quesnel B., Gautier P., Boulvais P., Cathelineau M., Maurizot P., Cluzel D., Ulrich M., Guillot S., Lesimple S. and Couteau C. (2013) Syn-tectonic, meteoric water-derived carbonation of the New Caledonia peridotite nappe. *Geology* **41**, 1063–1066.

Redlich K. A. (1909) Die Typen der Magnesitlagerstätten. *Z. Prakt. Geol.* **17**, 300–310.

Robinson G. R., Gosen B. S. Van and Foley N. K. (2006) Ultramafic-hosted Talc-Magnesite deposits. *42nd Forum Geol. Ind. Miner. May 7-13, 2006 Asheville, NC (USA). US Geol. Surv.*

Rose N. M., Rosing M. T. and Bridgwater D. (1996) The origin of metacarbonate rocks in the Archaean Isua supracrustal belt, West Greenland. *Am. J. Sci.* **296**, 1004–1044.

Rosenbaum J. and Sheppard S. M. . (1986) An isotopic study of siderites, dolomites and ankerites at high temperatures. *Geochim. Cosmochim. Acta* **50**, 1147–1150.

Rudge J. F., Kelemen P. B. and Spiegelman M. (2010) A simple model of reaction-induced cracking applied to serpentinization and carbonation of peridotite. *Earth Planet. Sci. Lett.* **291**, 215–227.

1672 Saenger C., Affek H. P., Felis T., Thiagarajan N., Lough J. M. and Holcomb M. (2012)
1673 Carbonate clumped isotope variability in shallow water corals: Temperature
1674 dependence and growth-related vital effects. *Geochim. Cosmochim. Acta* **99**, 224–
1675 242.
1676 Sanford R. (1982) Growth of Ultramafic Reaction Zones in Greenschist to Amphibolite
1677 Facies Metamorphism. *Am. J. Sci.* **282**, 543–616.
1678 Schauble E., Ghosh P. and Eiler J. (2006) Preferential formation of ^{13}C–^{18}O bonds in
1679 carbonate minerals, estimated using first-principles lattice dynamics. *Geochim.*
1680 *Cosmochim. Acta* **70**, 2510–2529.
1681 Schmid T. W. (2011) Clumped-isotopes - a new tool for old questions: case studies on
1682 biogenic and inorganic carbonates. Eidgenössische Technische Hochschule (ETH),
1683 Zürich, Switzerland.
1684 Schroll E. (2002) Genesis of magnesite deposits in the view of isotope geochemistry. *Bol.*
1685 *Parana. Geociências*, 59–68.
1686 Sena C. M., John C. M., Jourdan A.-L., Vandeginste V. and Manning C. (2014)
1687 Dolomitization of lower Cretaceous peritidal carbonates by modified seawater:
1688 constraints from clumped isotopic paleothermometry, elemental chemistry, and
1689 strontium isotopes. *J. Sediment. Res.* **84**, 552–566.
1690 Das Sharma S., Patil D. J. and Gopalan K. (2002) Temperature dependence of oxygen
1691 isotope fractionation of CO_2 from magnesite-phosphoric acid reaction. *Geochim.*
1692 *Cosmochim. Acta* **66**, 589–593.
1693 Sheppard S. M. F. (1986) Characterization and Isotopic Variations in Natural Waters. In
1694 *Stable Isotopes in High Temperature Geological Processes* (eds. J. W. Valley, H. P.
1695 Taylor Jr., and J. R. O'Neill). Mineral Soc America. pp. 165–183.
1696 Sheppard S. M. F. and Schwarcz H. P. (1970) Fractionation of carbon and oxygen
1697 isotopes and magnesium between coexisting metamorphic calcite and dolomite.
1698 *Contrib. to Mineral. Petrol.* **26**, 161–198.
1699 Sherlock R. and Logan M. (1995) Silica-carbonate Alteration of Serpentinite: Implication
1700 for the Association of Mercury and Gold Mineralization in Northern California.
1701 *Explor. Min. Geol.* **4**, 395–409.
1702 Stern L. A., Chamberlain C. P., Barnett D. E. and Ferry J. M. (1992) Stable isotope
1703 evidence for regional-scale fluid migration in a Barrovian metamorphic terrane,
1704 Vermont, USA. *Contrib. to Mineral. Petrol.* **112**, 475–489.
1705 Stolper D. A. and Eiler J. M. (2015) The kinetics of solid-state isotope-exchange
1706 reactions for clumped isotopes: A study of inorganic calcites and apatites from
1707 natural and experimental samples. *Am. J. Sci.* **315**, 363–411.
1708 Streit E., Kelemen P. and Eiler J. (2012) Coexisting serpentine and quartz from
1709 carbonate-bearing serpentinized peridotite in the Samail Ophiolite, Oman. *Contrib.*
1710 *to Mineral. Petrol.* **164**, 821–837.
1711 Suarez M. B., Passey B. H. and Kaakinen A. (2011) Paleosol carbonate multiple
1712 isotopologue signature of active East Asian summer monsoons during the late
1713 Miocene and Pliocene. *Geol.* **39** , 1151–1154.
1714 Sullivan N. C. (2014) Advances in samarium-neodymium geochronology: Applications
1715 to early Earth garnet, hydrothermal carbonate, and high temperature metamorphic
1716 systems. Ph.D. Thesis, Boston University.
1717 Swanson E. M., Wernicke B. P., Eiler J. M. and Losh S. (2012) Temperatures and fluids

on faults based on carbonate clumped-isotope thermometry. *Am. J. Sci.* **312**, 1–21.
Szilas K., Kelemen P. B. and Rosing M. T. (2015) The petrogenesis of ultramafic rocks in the >3.7Ga Isua supracrustal belt, southern West Greenland: Geochemical evidence for two distinct magmatic cumulate trends. *Gondwana Res.* **28**, 565–580.
Tang J., Dietzel M., Fernandez A., Tripati A. K. and Rosenheim B. E. (2014) Evaluation of kinetic effects on clumped isotope fractionation (Δ_{47}) during inorganic calcite precipitation. *Geochim. Cosmochim. Acta* **134**, 120–136.
Tripati A. K., Hill P. S., Eagle R. A., Mosenfelder J. L., Tang J., Schauble E. A., Eiler J. M., Zeebe R. E., Uchikawa J., Coplen T. B., Ries J. B. and Henry D. (2015) Beyond temperature: Clumped isotope signatures in dissolved inorganic carbon species and the influence of solution chemistry on carbonate mineral composition. *Geochim. Cosmochim. Acta* **166**, 344–371.
Trommsdorff V. and Evans B. W. (1977) Antigorite-Ophicarbonates: Phase Relations in a Portion of the System CaO-MgO-SiO_2-H_2O-CO_2. *Contrib. to Mineral. Petrol.* **56**, 39–56.
Ulrich M., Muñoz M., Guillot S., Cathelineau M., Picard C., Quesnel B., Boulvais P. and Couteau C. (2014) Dissolution–precipitation processes governing the carbonation and silicification of the serpentinite sole of the New Caledonia ophiolite. *Contrib. to Mineral. Petrol.* **167**, 952.
Vance D. and Holland T. (1993) A detailed isotopic and petrological study of a single garnet from the gassetts schist, Vermont. *Contrib. to Mineral. Petrol.* **114**, 101–118.
Vandeginste V., John C. M., Cosgrove J. W. and Manning C. (2014) Dimensions, texture-distribution, and geochemical heterogeneities of fracture–related dolomite geobodies hosted in Ediacaran limestones, northern Oman. *Am. Assoc. Pet. Geol. Bull.* **98**, 1789–1809.
Vasconcelos C., McKenzie J. A., Warthmann R. and Bernasconi S. M. (2005) Calibration of the $\delta^{18}O$ paleothermometer for dolomite precipitated in microbial cultures and natural environments. *Geology* **33**, 317–320.
Wacker U., Fiebig J. and Schoene B. R. (2013) Clumped isotope analysis of carbonates: comparison of two different acid digestion techniques. *Rapid Commun. Mass Spectrom.* **27**, 1631–42.
Wacker U., Fiebig J., Tödter J., Schöne B. R., Bahr A., Friedrich O., Tütken T., Gischler E. and Joachimski M. M. (2014) Empirical calibration of the clumped isotope paleothermometer using calcites of various origins. *Geochim. Cosmochim. Acta* **141**, 127–144.
Wang A., Pasteris J. D., Meyer H. O. A. and Dele-Duboi M. L. (1996) Magnesite-bearing inclusion assemblage in natural diamond. *Earth Planet. Sci. Lett.* **141**, 293–306.
Wang Z., Schauble E. A. and Eiler J. M. (2004) Equilibrium thermodynamics of multiply substituted isotopologues of molecular gases. *Geochim. Cosmochim. Acta* **68**, 4779–4797.
Wenner D. B. and Taylor H. P. (1971) Temperatures of serpentinization of ultramafic rocks based on O^{18}/O^{16} fractionation between coexisting serpentine and magnetite. *Contrib. to Mineral. Petrol.* **32**, 165–185.
White D., Barnes I. and O'Neil J. (1973) Thermal and Mineral Waters of Nonmeteoric Origin, California Coast Ranges. *Geol. Soc. Am. Bull.* **84**, 547–560.
Wilson S. A., Barker S. L. L., Dipple G. M. and Atudorei V. (2010) Isotopic

disequilibrium during uptake of atmospheric CO_2 into mine process waters: Implications for CO_2 sequestration. *Environ. Sci. Technol.* **44**, 9522–9529.

Wilson S. A., Dipple G. M., Power I. M., Thom J. M., Anderson R. G., Raudsepp M., Gabites J. E. and Southam G. (2009) Carbon Dioxide Fixation within Mine Wastes of Ultramafic-Hosted Ore Deposits: Examples from the Clinton Creek and Cassiar Chrysotile Deposits, Canada. *Econ. Geol.* **104** , 95–112.

Wilson S. A., Harrison A. L., Dipple G. M., Power I. M., Barker S. L. L., Ulrich M. K., Fallon S. J., Raudsepp M. and Southam G. (2014) Offsetting of CO_2 emissions by air capture in mine tailings at the Mount Keith Nickel Mine, Western Australia: Rates, controls and prospects for carbon neutral mining. *Int. J. Greenh. Gas Control* **25**, 121–140.

Winnick M. J., Chamberlain C. P., Caves J. K. and Welker J. M. (2014) Quantifying the isotopic "continental effect." *Earth Planet. Sci. Lett.* **406**, 123–133.

Wise W. and Moller W. (1995) Geology and Mineralogy of the New Idria District: San Benito and Fresno Counties, California. *Rocks Miner.* **70.1**, 30–35.

Zachmann D. and Johannes W. (1989) Cryptocrystaline Magnesite. In *Magnesite. Geology, Mineralogy, Geochemistry, Formation of Mg-Carbonates* (ed. P. Moller). Gebruder Borntraeger, Berlin-Stuttgart. pp. 15–28.

Zedef V., Russell M. J., Fallick A. E. and Hall A. J. (2000) Genesis of vein stockwork and sedimentary magnesite and hydromagnesite deposits in the ultramafic terranes of southwestern Turkey: A stable isotope study. *Econ. Geol.* **95**, 429–445.

Zhang R. and Liou J. (1994) Significance of magnesite paragenesis in ultrahigh-pressure metamorphic rocks. *Am. Mineral.* **79**, 397–400.

Van Zuilen M. A., Lepland A., Teranes J., Finarelli J., Wahlen M. and Arrhenius G. (2003) Graphite and carbonates in the 3.8 Ga old Isua Supracrustal Belt, southern West Greenland. *Precambrian Res.* **126**, 331–348.

Table 1

Table 1 Mineralogy, mode of formation, location, and inferred geologic or known temperature of magnesium carbonate formation

Sample	Mineralogy (*)	Type	Location	Geologic / Experimental Temperature (°C)
Red Mountain cryptocrystalline magnesite (California)				
SD10-2	magnesite	massive vein	Outcrop 37°24'48.4"N, 121°28'08.9"W. 3520 ft. (1073 m) level	10 to 100°C (2)
DV10-27C	magnesite	massive vein	Adit entrance 37°24'41.6"N, 121°28'15.9"W, 3240 ft. (988 m) level. 714 ft. (218 m) from entrance. [5400 N, 4500 W Plate 42] (1)	10 to 100°C (2)
DV10-21B	magnesite	stockwork vein	Adit entrance 37°24'41.6"N, 121°28'15.9"W. 3240 ft. (988 m) level. 750 ft. (229 m) from entrance to the right. [5700 N and 4400 W Plate 42] (1)	10 to 100°C (2)
DV10-21A	magnesite	nodule	Adit entrance 37°24'41.6"N, 121°28'15.9"W. 3240 ft. (988 m) level. 750 ft. (229 m) from entrance to the right. [5700 N and 4400 W Plate 42] (1)	10 to 100°C (2)
N6V-2A	magnesite	nodule	Adit entrance 37°24'41.3"N, 121°27'51.0"W. 3230 ft. (985 m) level. 226 ft. (69 m) from entrance to the left. [4800 N and 2000 W Plate 46] (1)	10 to 100°C (2)
RM-09-12-II	magnesite	breccia matrix	Float sample; magnesite breccia with pink and purple matrix	10 to 100°C (2)
DV10-6	magnesite	massive vein	Outcrop 37°24'49.0"N, 121°28'13.9"W. 3590 ft. (1094 m) level; highest point of Red Mountain deposit	10 to 100°C (2)
Worldwide cryptocrystalline magnesite deposits				
AU-15	magnesite	vein	Kraubath (Austria)	13 to 42°C (3)
070815-7	magnesite	vein	Eskişehir (Turkey)	37.9 to 80°C (3)
dhs23	magnesite	vein	Derakht-Senjed (Iran)	20 to 44°C (3)
Surface hydrous magnesium carbonates				
MCL-2	hydromagnesite	nodule	McLaughin serpentinite (California, USA) 38°48'20.92"N, 122°22'57.82"W	35 to −2°C (4)
RC1	hydromagnesite	nodule	Del Puerto peridotite roadcut (California, USA) 37°24'37.10"N, 121°25'40.76"W	35 to −3°C (4)
09-NI-3	hydromagnesite	nodule	New Idria serpentinite (California, USA) 36°24'04.40"N, 120°40'32.76"W	40 to −8°C (4)
10-NI-1	artinite	acicular cluster	New Idria serpentinite (California, USA) 36°21'16.89"N, 120°40'34.99"W	40 to −8°C (4)
Red Mountain mine adit coatings				
DPT12-10 Crust (■)	hydromagnesite minor dypingite	crustiform	Red Mountain mine adit (California, USA); Adit entrance 37°24'39.12"N, 121°28'18.75"W. 3040 ft. (927 m) level	11.3 ± 0.1°C (5)
DPT12-10 Salt	nesquehonite	crustiform	Red Mountain mine adit (California, USA); Adit entrance 37°24'39.12"N, 121°28'18.75"W. 3040 ft. (927 m) level	11.3 ± 0.1°C (5)
High-temperature carbonates				
14-05-Red (■)	magnesite	vein	Isua (Greenland) 65°7'51.96"N, 50°9'59.94"	430 to 490°C (6)
14-05-White	dolomite	vein	Isua (Greenland) 65°7'51.96"N, 50°9'59.94"	430 to 490°C (6)
08SVT-4A	dolomite	vein	Talc mine in serpentinized peridotite (Ludlow, Vermont, USA)	430 to 490°C (6)
Olivine-magnesite experiments				
0209 (■)	olivine magnesite	spiral growth	lab experiment	60°C (7)
1210P (■)	olivine magnesite	spiral growth	lab experiment	60°C (7)
Hydromagnesite experiments				
Mg-1 (■)	Hydromagnesite, minor aragonite	flakes	lab experiment	79.9 ± 0.1°C (8)
Mg-3 (■)	hydromagnesite	flakes	lab experiment	79.9 ± 0.1°C (8)

(*) Determined via powder XRD. Refer to Fig. A1 for diffractograms of selected samples

(1) Plate number and coordinates in [brackets] refer to mining maps in Bodenlos (1950)

(2) Stable isotope thermometry assuming $\delta^{18}O_{fluid}$ compositions (Barnes *et al* . 1973)

(3) Austria: Kralik (1989); Turkey: Kahya and Kuşcu (2014) and Ece *et al* . (2005): Iran, Mirnejad *et al* . (2008)

(4) Based on yearly averages from nearby weather stations shown in Fig. 1b. Data on Figs. A4 and A5

(5) Constant temperature inside the mine measured throughout the day on 25 February 2012 (Fig. 5)

(6) Based on stability of coexisiting dolomite+magnesite+talc (Bucher and Grapes, 2011)

(7) Controlled laboratory temperatures (Johnson *et al* ., 2014)

(8) Controlled laboratory temperatures (Kluge and John, 2015)

(■) Sample used for acid fractionation evaluation (Section 4.1)

Table 2

Table 2 Δ_{47}, clumped-isotope temperatures, $\delta^{18}O$, and $\delta^{13}C$ values of natural and laboratory magnesium carbonate samples.

Sample	replicates	Δ_{47} (raw) not acid corrected (‰)	1SD	Δ_{47} acid corrected (‰) (1)	T (°C)	Uncertainty (°C)	$\delta^{13}C$ (raw) (‰) VPDB	1SD	$\delta^{18}O$ (raw) (‰)	1SD	$\delta^{18}O$ acid corrected (‰) (2) VSMOW
Red Mountain cryptocrystalline magnesite (California)											
SD10-2	6	0.609	0.012	0.678	31.6	1.8	-11.30	0.00	37.72	0.09	28.00
DV10-27C	3	0.623	0.003	0.692	26.8	0.7	-10.63	0.18	36.53	0.22	26.82
DV10-21B	3	0.655	0.024	0.724	15.9	4.5	-10.73	0.07	37.62	0.13	27.90
DV10-21A	3	0.619	0.010	0.688	28.1	2	-10.53	0.09	36.96	0.06	27.25
N6V-2A	3	0.650	0.016	0.719	17.5	3.1	-10.78	0.16	36.98	0.36	27.27
RMO-09-12-II	1	0.633		0.702	23.2	6.7	-12.21	0.10	36.48	0.20	26.77
DV10-6	3	0.642	0.034	0.711	20.2	6.4	-11.79	0.20	37.35	0.53	27.63
Worldwide cryptocrystalline magnesite deposits											
AU-15	2	0.619	0.010	0.688	28.2	2.5	-14.57	0.01	36.23	0.14	26.52
070815-7	2	0.631	0.022	0.700	24	5.2	-10.52	0.06	37.06	0.07	27.35
dhs23	3	0.638	0.039	0.707	21.7	8	-4.95	0.60	33.53	1.27	23.85
Surface hydrous magnesium carbonates											
MCL-2	3	0.635	0.019	0.704	22.7	3.8	-13.69	0.01	36.99	0.03	27.28
RC1	2	0.660	0.002	0.729	14.2	0.5	-7.26	0.07	37.77	0.17	28.05
09-NI-3	3	0.639	0.018	0.708	21.1	3.4	-13.33	0.08	35.62	0.13	25.92
10-NI-1	2	0.636	0.015	0.705	22.1	3.5	-5.69	0.46	35.26	0.72	25.56
Red Mountain mine adit coatings											
DPT12-10 Crust	2	0.653	0.006	0.722	16.7	1.5	3.94	0.01	41.41	0.19	31.65
DPT12-10 Salt	2	0.586	0.013	0.655	40.2	3.8	7.31	0.59	42.16	0.51	32.40
High-temperature carbonates											
14-05 Red	3	0.254	0.011	0.323	490	+60 −40	-3.10	0.11	16.47	0.19	7.11
14-05 White	3	0.289	0.011	0.358	326	20	-3.27	0.06	15.78	0.13	6.27
08SVT-4A	2	0.279	0.021	0.348	360	+70 −50	-12.85	0.05	20.35	0.02	10.95
Olivine-magnesite experiments											
0209	4	0.573	0.025	0.642	45.6	4.8	0.80	0.29	20.03	0.57	10.47
1210P	1	0.572		0.641	45.9	7.9	-45.32	0.20	21.19	0.20	11.62
Hydromagnesite experiments											
Mg-1	3	0.499	0.010	0.568	79.9	2.8	-17.70	0.06	-16.96	0.27	13.54
Mg-3	4	0.502	0.023	0.571	78.4	5.8	-16.76	0.01	-16.14	0.01	14.33

SD=Standard deviation

(1) Acid correction value (0.069‰) for Δ_{47} compositions from Kluge et al. (2015)

(2) Acid correction at digestion temperature 90°C from Das Sharma et al. (2002)

Table 3

Table 3 Calculated $\delta^{18}O_{water}$ and $\delta^{13}C_{CO2}$ of mineralizing fluids using the respective clumped-isotope temperature

Sample	Clumped T (°C)	uncertainty (°C)	$\delta^{18}O$ (‰) (1) VSMOW	α (1)	$\delta^{18}O$ water (‰) (1) VSMOW	α (2)	$\delta^{18}O$ water (‰) (2) VSMOW	α (3)	$\delta^{18}O$ water (‰) (3) VSMOW	α (4)	$\delta^{18}O$ water (‰) (4) VSMOW	α (5)	$\delta^{18}O$ water (‰) (5) VSMOW	α (6)	$\delta^{13}C$ $CO_{2(g)}$ (‰) (6) VPDB	α (7)	$\delta^{13}C$ $CO_{2(g)}$ (‰) (7) VPDB
Red Mountain cryptocrystalline magnesite (California)																	
SD10-2	31.6	1.8	28.00	1.0350	**-6.8**	1.0300	-2.0	1.0291	-1.1	1.0388	-10.4	1.0308	N.A.	1.0117	**-22.7**	1.0196	-30.3
DV10-27C	26.8	0.7	26.82	1.0363	**-9.1**	1.0311	-4.2	1.0301	-3.2	1.0401	-12.8	1.0318	N.A.	1.0124	**-22.7**	1.0203	-30.3
DV10-21B	15.9	4.5	27.90	1.0394	**-11.1**	1.0337	-5.6	1.0325	-4.4	1.0431	-14.6	1.0342	N.A.	1.0141	**-24.5**	1.0222	-32.2
DV10-21A	28.1	2	27.25	1.0359	**-8.4**	1.0308	-3.5	1.0298	-2.5	1.0398	-12.0	1.0315	N.A.	1.0122	**-22.4**	1.0201	-30.0
N6V-2A	17.5	3.1	27.27	1.0389	**-11.2**	1.0333	-5.8	1.0321	-4.7	1.0427	-14.8	1.0338	N.A.	1.0139	**-24.3**	1.0219	-32.0
RMO-09-12-II	23.2	6.7	26.77	1.0373	**-10.1**	1.0319	-5.0	1.0308	-3.9	1.0411	-13.7	1.0325	N.A.	1.0129	**-24.8**	1.0209	-32.5
DV10-6	20.2	6.4	27.63	1.0382	**-10.1**	1.0326	-4.9	1.0315	-3.7	1.0419	-13.7	1.0332	N.A.	1.0134	**-24.9**	1.0214	-32.5
Worldwide cryptocrystalline magnesite deposits																	
AU-15	28.2	2.5	26.52	1.0359	**-9.1**	1.0308	-4.1	1.0298	-3.2	1.0397	-12.7	1.0315	N.A.	1.0122	**-26.4**	1.0201	-34.0
070815-7	24	5.2	27.35	1.0371	**-9.4**	1.0317	-4.3	1.0307	-3.2	1.0409	-13.0	1.0324	N.A.	1.0128	**-23.0**	1.0208	-30.7
dhs23	21.7	8	23.85	1.0377	**-13.4**	1.0323	-8.2	1.0312	-7.1	1.0415	-16.9	1.0329	N.A.	1.0132	**-17.9**	1.0212	-25.6
Surface hydrous magnesium carbonates																	
MCL-2	22.7	3.8	27.28	1.0374	-9.8	1.0320	-4.6	1.0327	**-5.2**	1.0412	-13.4	1.0327	N.A.	1.0130	**-26.3**	1.0210	-34.0
RC1	14.2	0.5	28.05	1.0399	-11.4	1.0341	-5.9	1.0346	**-6.3**	1.0436	-14.9	1.0346	N.A.	1.0144	**-21.4**	1.0225	-29.1
09-NI-3	21.1	3.4	25.92	1.0379	-11.5	1.0324	-6.3	1.0330	**-6.9**	1.0417	-15.1	1.0330	N.A.	1.0133	**-26.2**	1.0213	-33.9
10-NI-1	22.1	3.5	25.56	1.0376	-11.6	1.0322	-6.4	1.0328	**-7.0**	1.0414	-15.2	1.0328	N.A.	1.0131	**-18.5**	1.0211	-26.2
Red Mountain mine adit coatings																	
DPT12-10 Crust	16.7	1.5	31.65	1.0392	-7.2	1.0335	-1.8	1.0340	-2.3	1.0429	-10.8	1.0340	N.A.	1.0140	-9.9	1.0221	-17.7
DPT12-10 Salt	40.2	3.8	32.40	1.0329	-0.5	1.0283	4.0	1.0292	3.2	1.0367	-4.1	1.0292	N.A.	1.0105	-3.1	1.0183	-10.8
High-temperature carbonates																	
14-05 Red	490	+60 −40	7.11	1.0025	**4.6**	1.0029	4.2	1.0039	3.2	0.9981	9.0	1.0056	N.A.	0.9980	**-1.1**	1.0019	-5.0
14-05 White	326	20	6.27	1.0074	-1.1	1.0061	0.2	1.0068	-0.6	1.0019*	4.4	1.0085	-2.2	0.9987	-1.9	1.0026	N.A.
08SVT-4A	360	+70 −50	10.95	1.0066	4.3	1.0052	5.7	1.0060	4.9	1.0005*	10.4	1.0077	**3.2**	0.9984	**-11.3**	1.0024	N.A.
Olivine-magnesite experiments																	
0209	45.6	4.8	10.47	1.0317	-20.5	1.0272	-16.3	1.0265	-15.6	1.0354	-24.3	1.0282	-17.2	1.0098	-8.9	1.0175	-16.4
1210P	45.9	7.9	11.62	1.0316	-19.4	1.0272	-15.2	1.0264	-14.4	1.0353	-23.1	1.0281	-16.1	1.0098	-54.6	1.0175	-61.7
Hydromagnesite experiments																	
Mg-1	79.9	2.8	13.54	1.0231	-9.3	1.0217	-8.0	1.0214	-7.7	1.0283	-14.4	1.0231	-9.3	1.0064	-23.9	1.0135	-30.8
Mg-3	78.4	5.8	14.33	1.0231	-8.5	1.0219	-7.4	1.0216	-7.1	1.0286	-13.8	1.0233	-8.7	1.0065	-23.1	1.0137	-30.0

Bolded values are used in the discussion and to construct Fig. 10b

(1) α and $\delta^{18}O_{water}$ from Aharon (1988) [Dolomite included] Magnesite

(2) α and $\delta^{18}O_{water}$ from Aharon (1988) [Dolomite excluded] Magnesite

(3) α and $\delta^{18}O_{water}$ from Aharon (1988) Hydromagnesite

(4) α and $\delta^{18}O_{water}$ from Chacko and Deines (2008) Magnesite (*Dolomite)

(5) α and $\delta^{18}O_{water}$ from Vasconcelos (2005) Dolomite

(6) α and $\delta^{13}C$ $CO_{2(gas)}$ from Aharon (1988) Magnesite and Dolomite

(7) α and $\delta^{13}C$ $CO_{2\ (gas)}$ from Golyshev et al. (1981) Magnesite

Figure 1

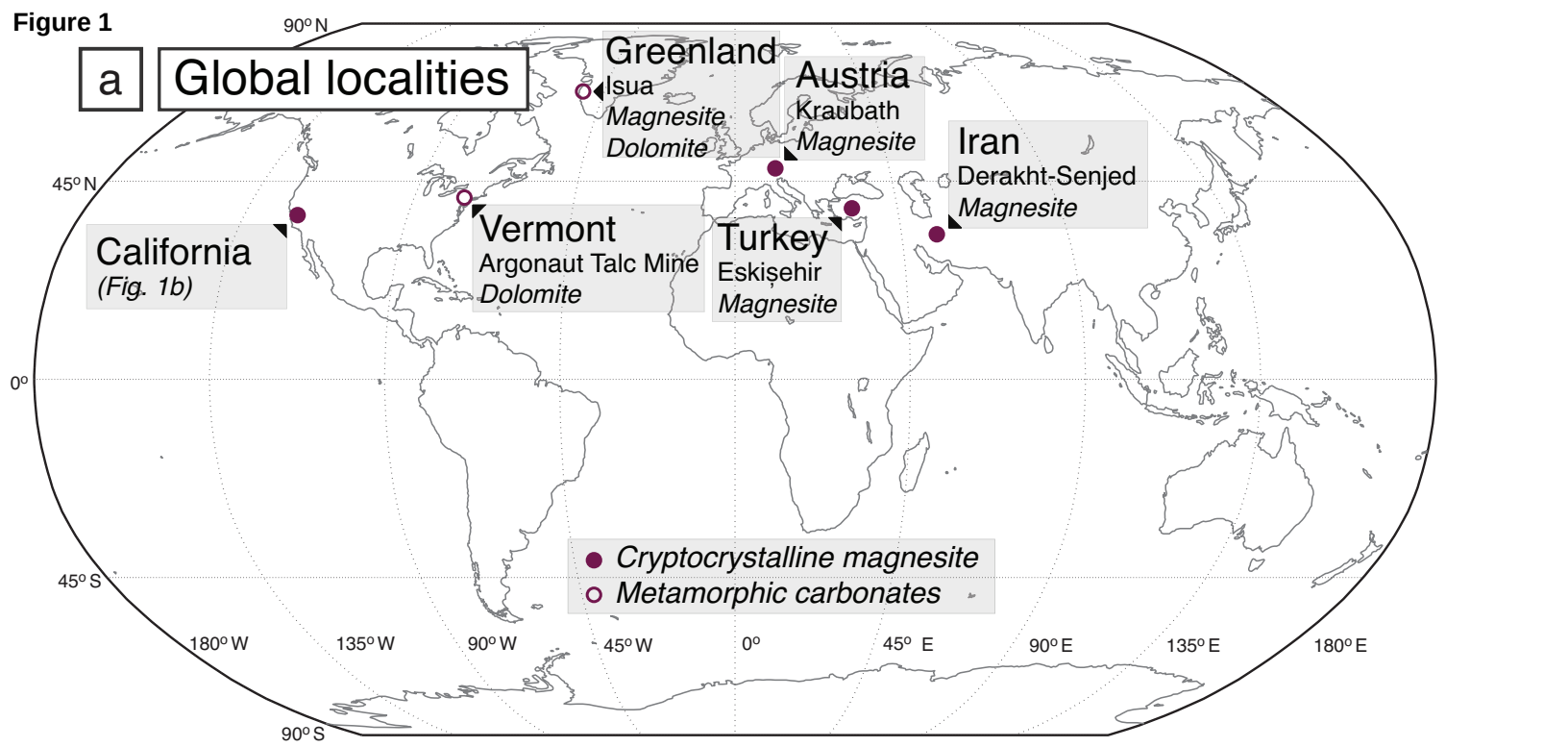
a
Global localities
Greenland
Isua
Magnesite
Dolomite
Austria
Kraubath
Magnesite
Iran
Derakht-Senjed
Magnesite
California
(Fig. 1b)
Vermont
Argonaut Talc Mine
Dolomite
Turkey
Eskişehir
Magnesite
Cryptocrystalline magnesite
Metamorphic carbonates
90° N
45° N
0°
45° S
90° S
180° W
135° W
90° W
45° W
0°
45° E
90° E
135° E
180° E

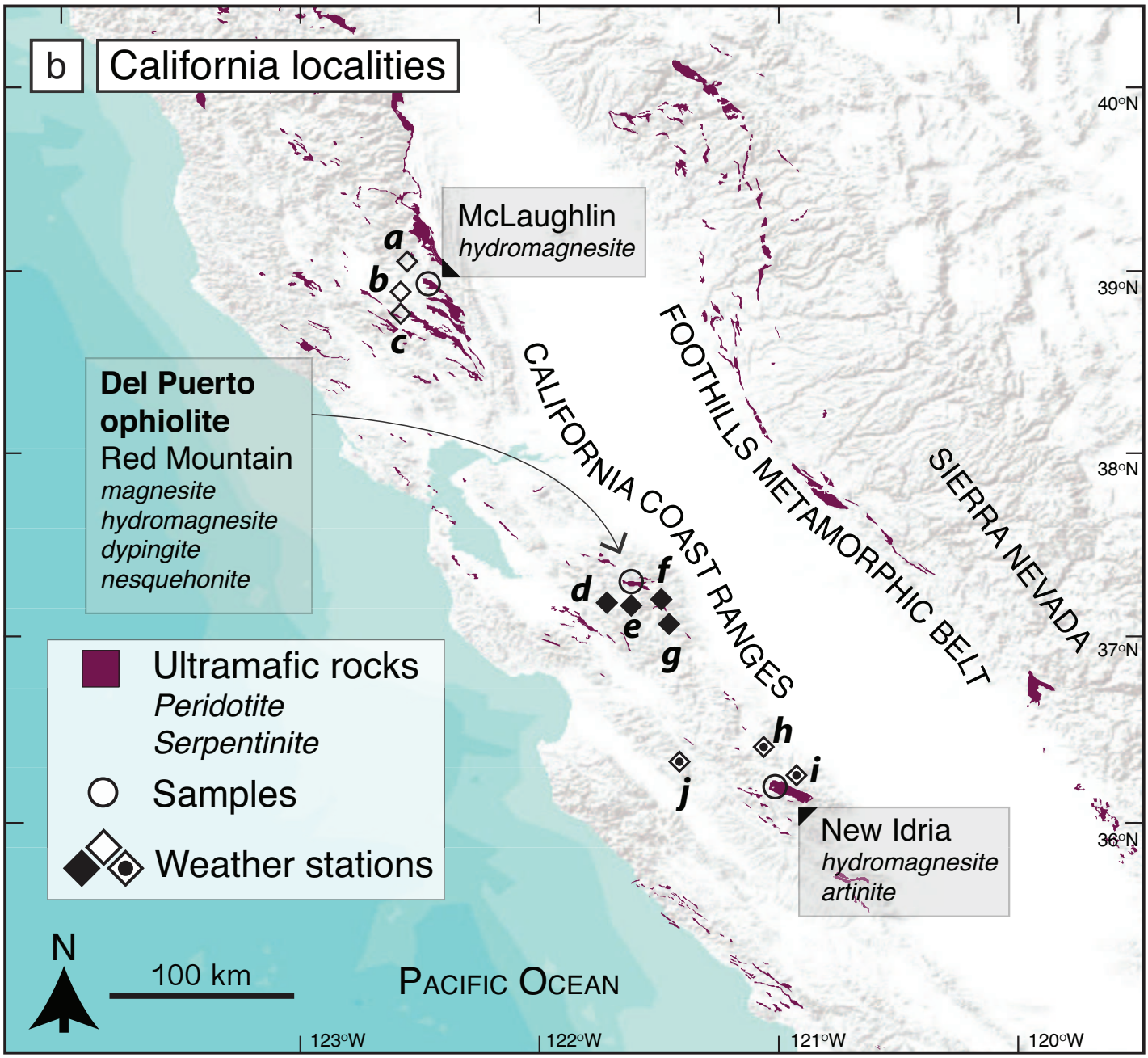
b
California localities
McLaughlin
hydromagnesite
a
b
c
Del Puerto
ophiolite
Red Mountain
magnesite
hydromagnesite
dypingite
nesquehonite
CALIFORNIA COAST RANGES
FOOTHILLS METAMORPHIC BELT
SIERRA NEVADA
d
e
f
g
h
i
j
New Idria
hydromagnesite
artinite
Ultramafic rocks
Peridotite
Serpentinite
Samples
Weather stations
N
100 km
PACIFIC OCEAN
40°N
39°N
38°N
37°N
36°N
123°W
122°W
121°W
120°W

Figure 2

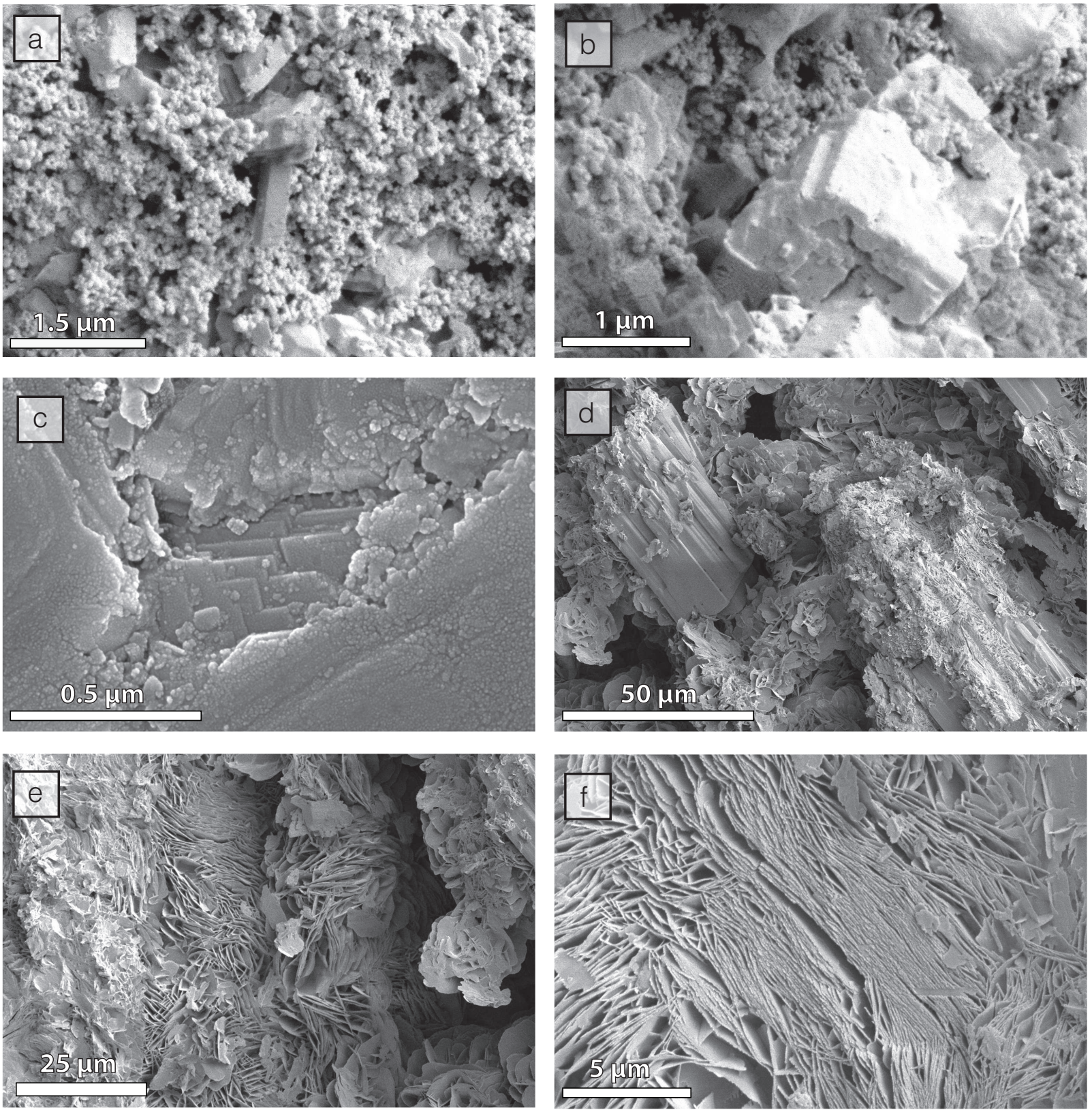

Figure 3

Click here to download high resolution image

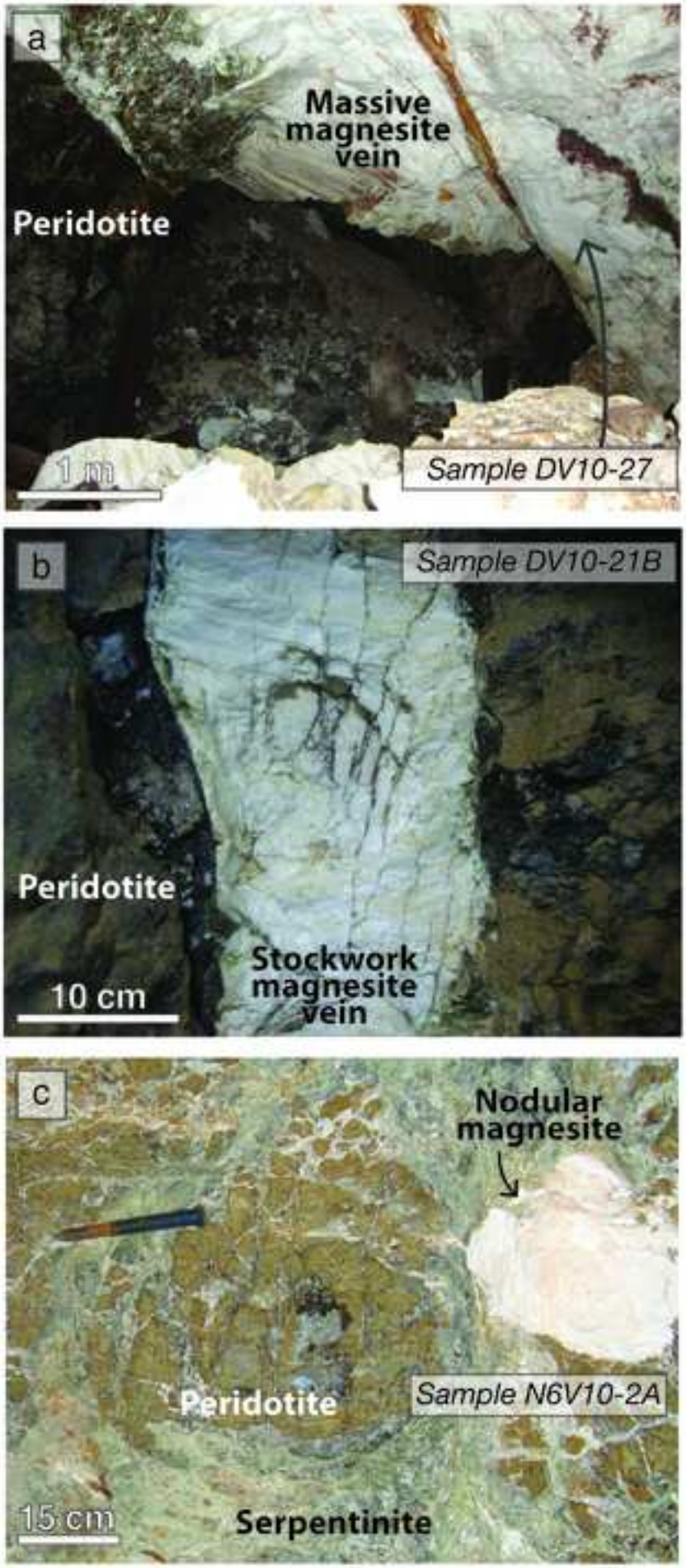

Figure 4

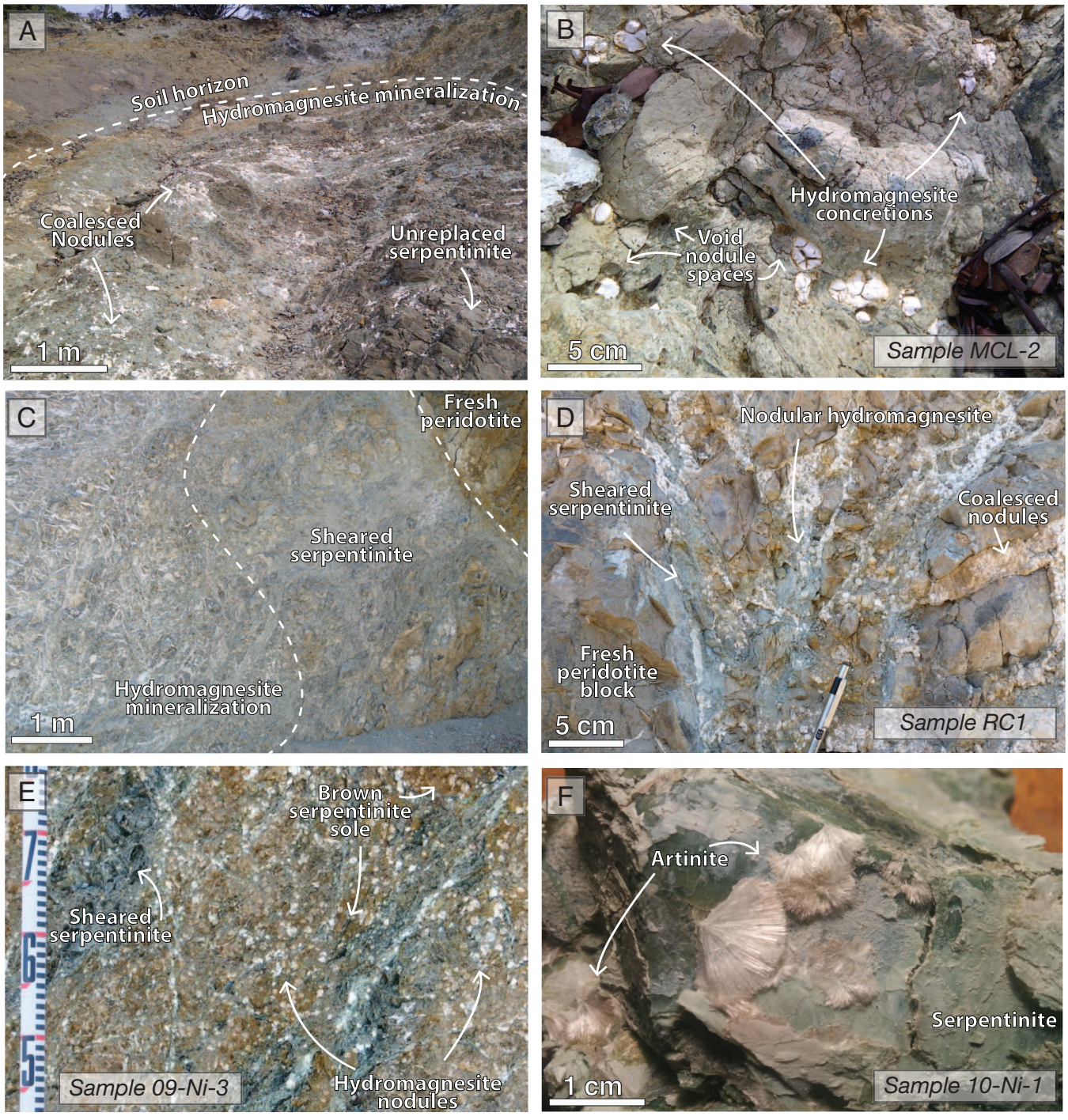
A
Soil horizon
Hydromagnesite mineralization
Coalesced Nodules
Unreplaced serpentinite
1 m
B
Hydromagnesite concretions
Void nodule spaces
5 cm
Sample MCL-2
C
Fresh peridotite
Sheared serpentinite
Hydromagnesite mineralization
1 m
D
Nodular hydromagnesite
Sheared serpentinite
Coalesced nodules
Fresh peridotite block
5 cm
Sample RC1
E
Brown serpentinite sole
Sheared serpentinite
Sample 09-Ni-3
Hydromagnesite nodules
F
Artinite
Serpentinite
1 cm
Sample 10-Ni-1

Figure 5

Click here to download high resolution image

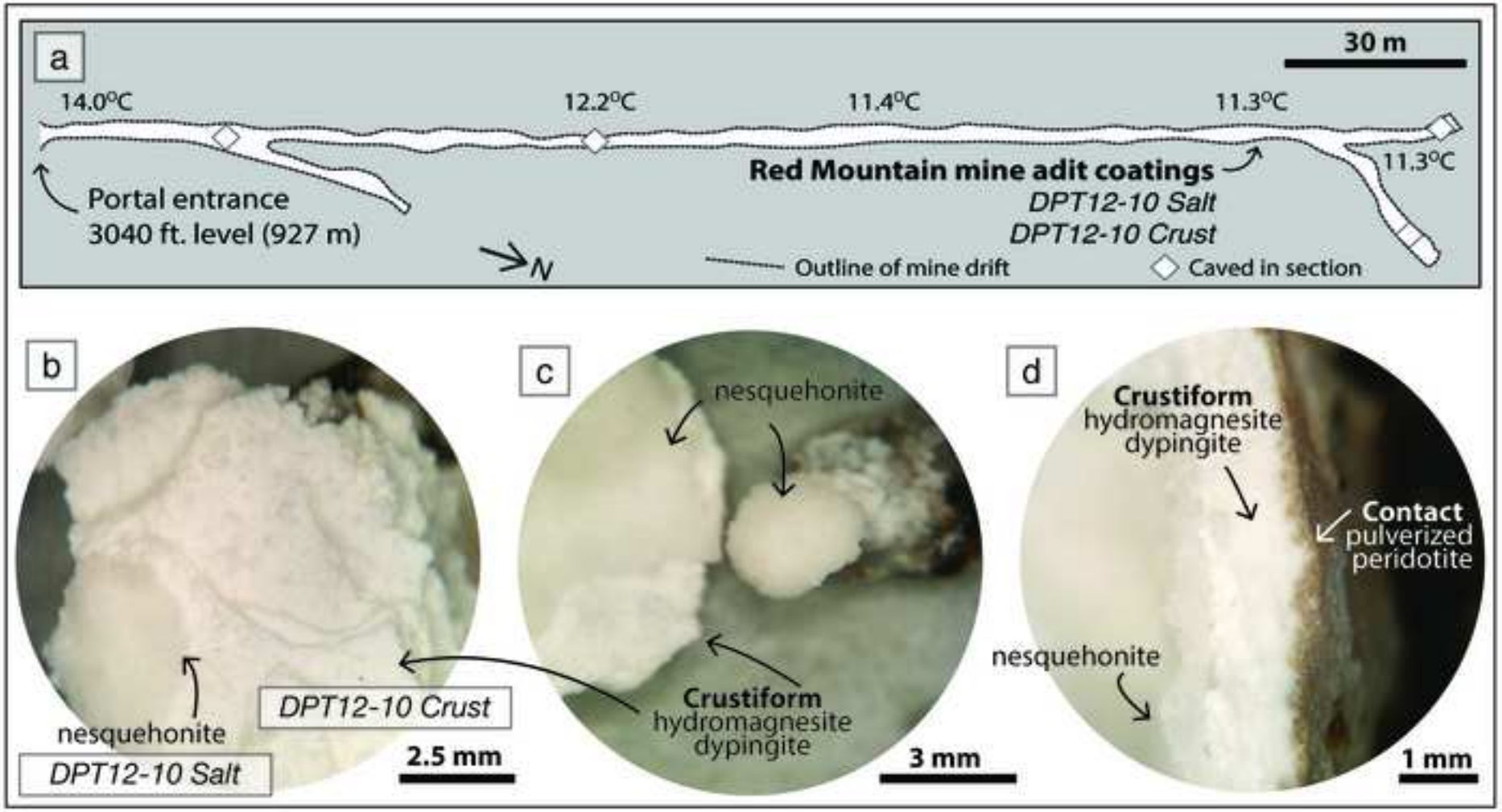

Figure 6

Click here to download high resolution image

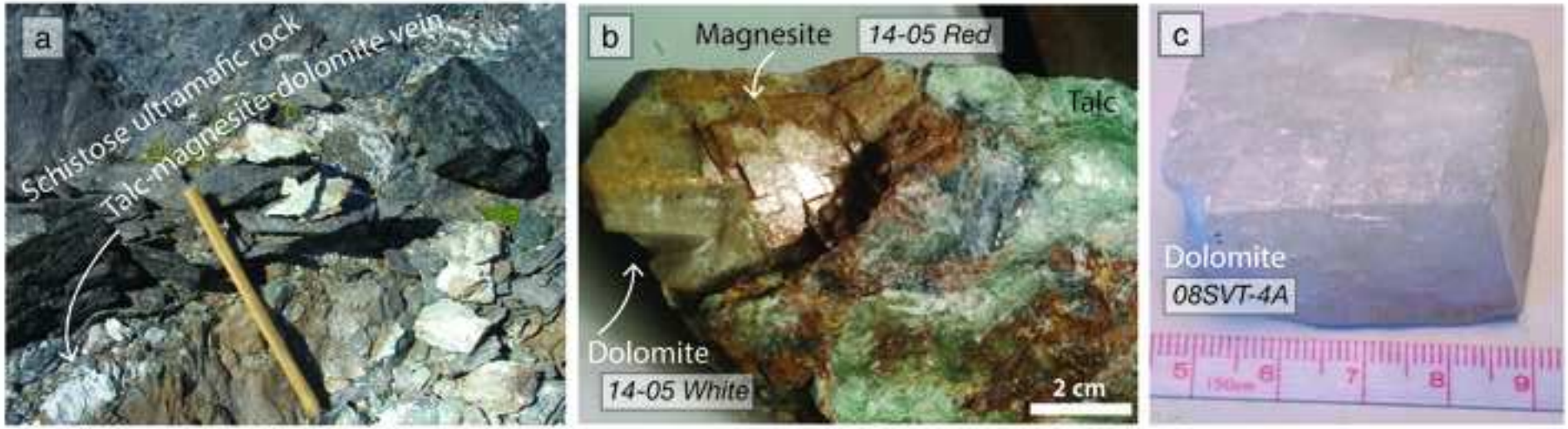

Figure 7

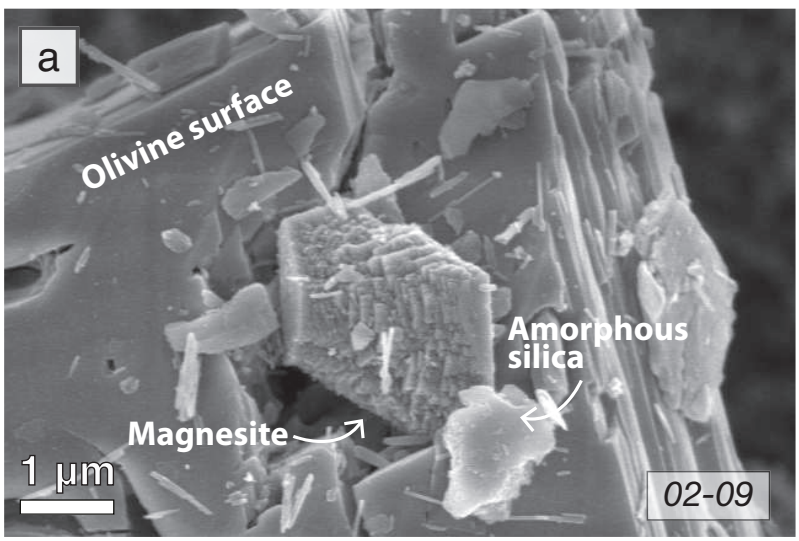
a
Olivine surface
Amorphous silica
Magnesite
1 µm
02-09

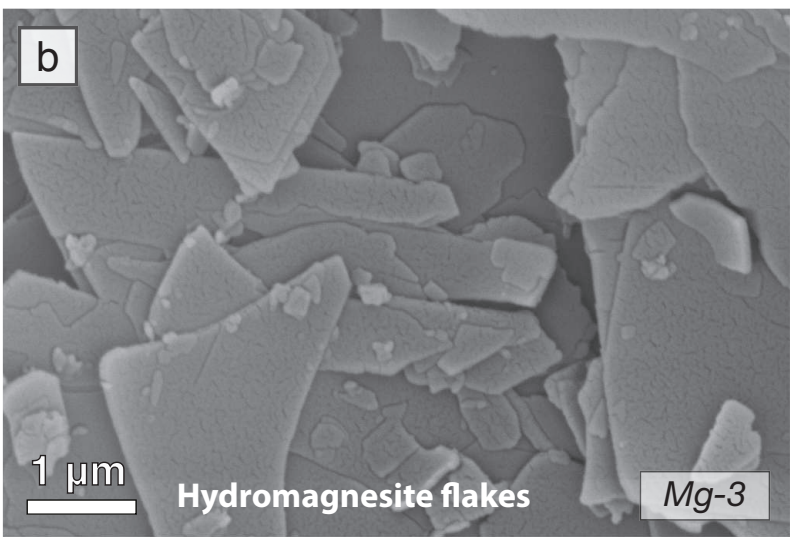
b
1 µm
Hydromagnesite flakes
Mg-3

Figure 8

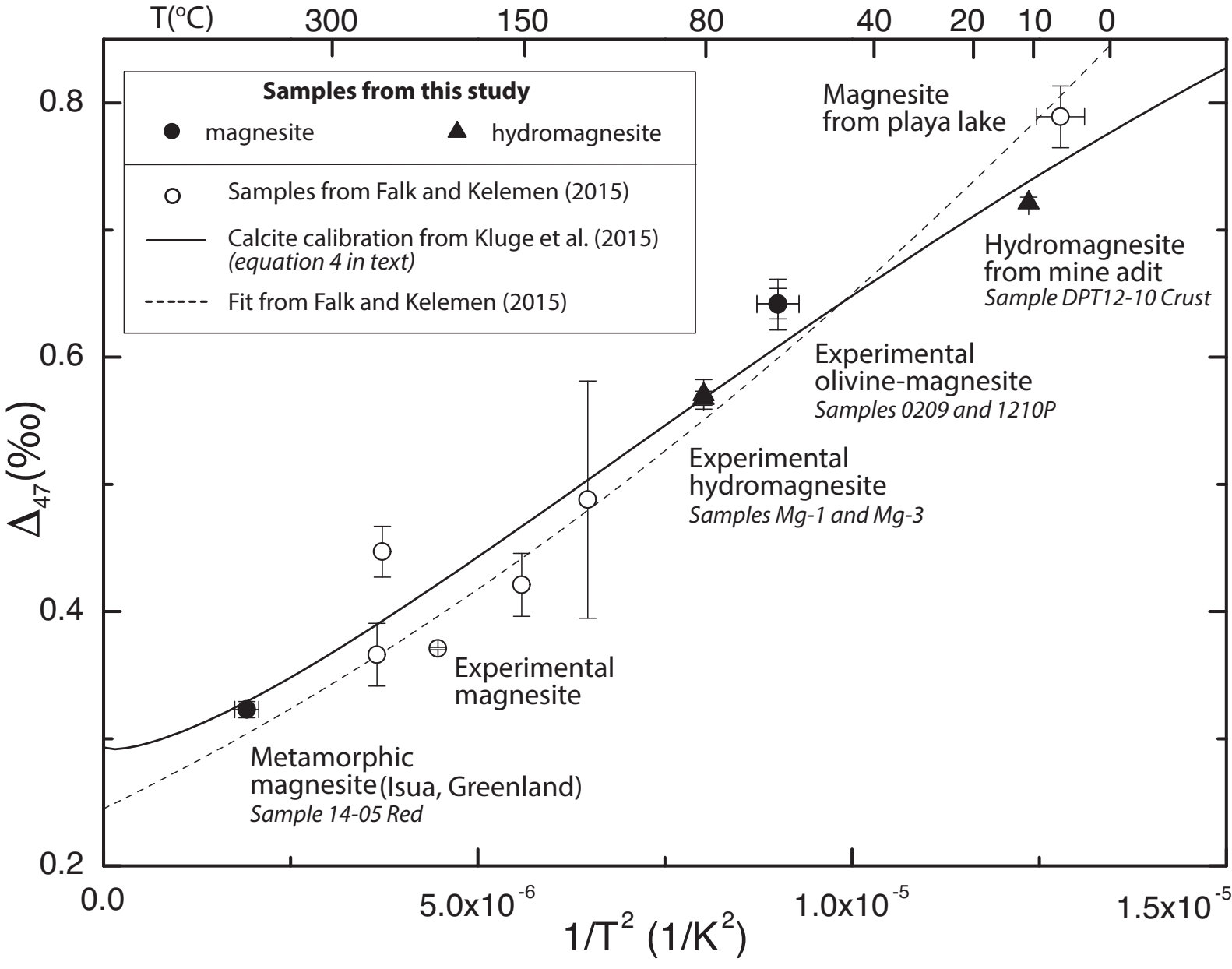
T(°C)
300
150
80
40
20
10
0
Samples from this study
magnesite
hydromagnesite
Samples from Falk and Kelemen (2015)
Calcite calibration from Kluge et al. (2015)
(equation 4 in text)
Fit from Falk and Kelemen (2015)
Magnesite
from playa lake
Hydromagnesite
from mine adit
Sample DPT12-10 Crust
Experimental
olivine-magnesite
Samples 0209 and 1210P
Experimental
hydromagnesite
Samples Mg-1 and Mg-3
Experimental
magnesite
Metamorphic
magnesite (Isua, Greenland)
Sample 14-05 Red
0.8
0.6
0.4
0.2
Δ47 (‰)
0.0
5.0x10-6
1.0x10-5
1.5x10-5
1/T2 (1/K2)

Figure 9

Click here to download high resolution image

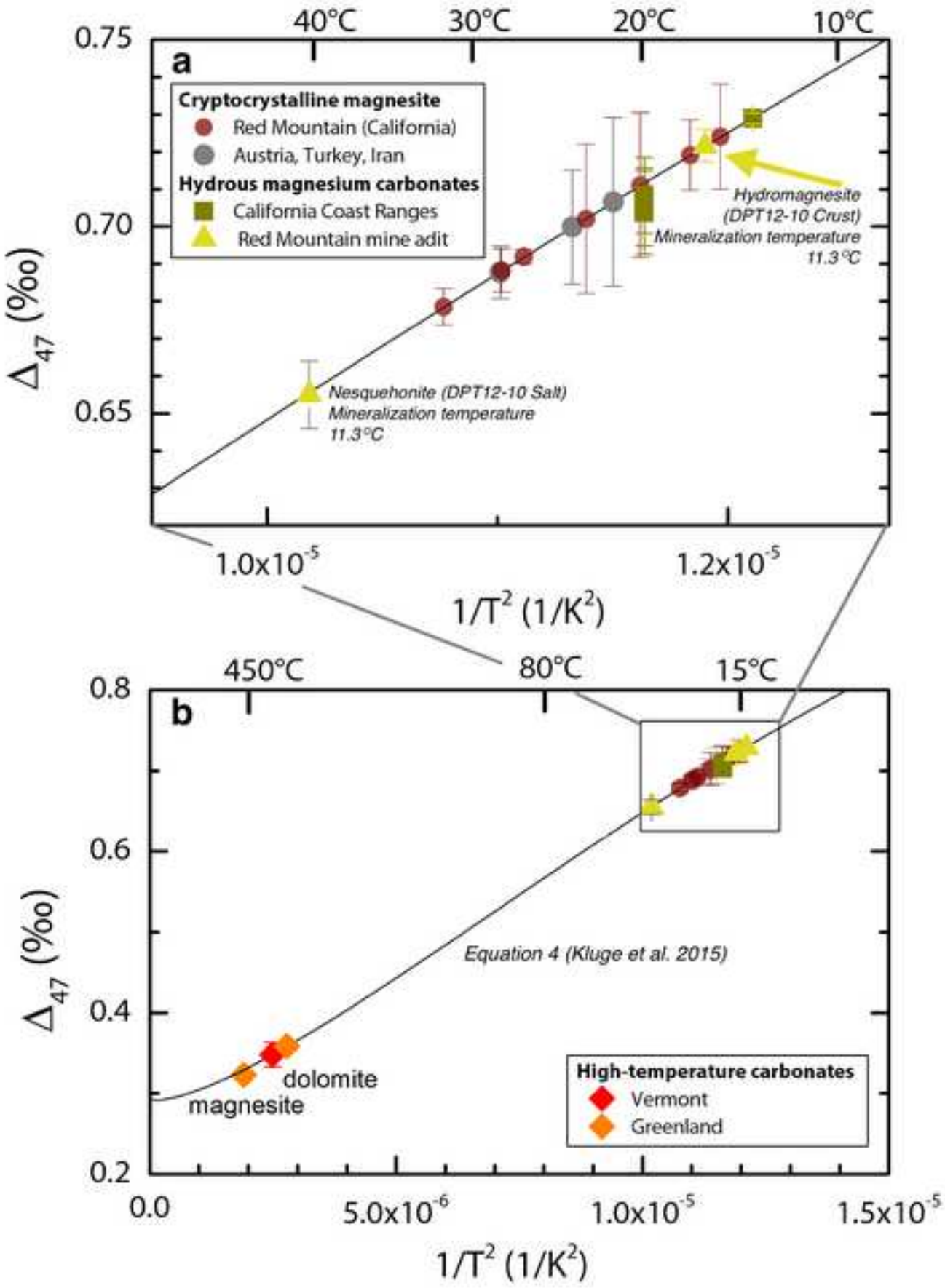

Figure 10

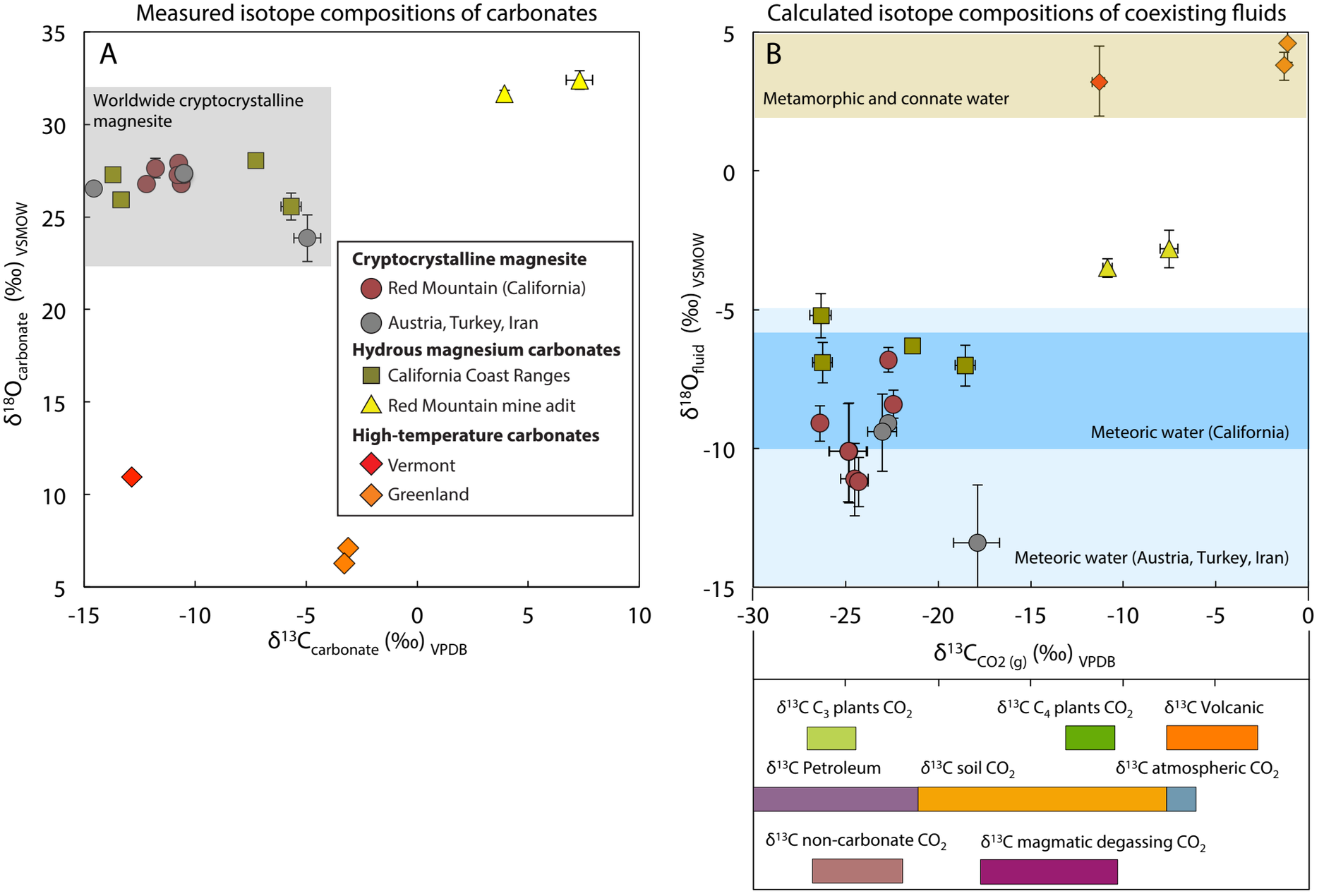
Measured isotope compositions of carbonates
A
Worldwide cryptocrystalline magnesite
Cryptocrystalline magnesite
Red Mountain (California)
Austria, Turkey, Iran
Hydrous magnesium carbonates
California Coast Ranges
Red Mountain mine adit
High-temperature carbonates
Vermont
Greenland
δ18Ocarbonate (‰) VSMOW
δ13Ccarbonate (‰) VPDB
Calculated isotope compositions of coexisting fluids
B
Metamorphic and connate water
Meteoric water (California)
Meteoric water (Austria, Turkey, Iran)
δ18Ofluid (‰) VSMOW
δ13CCO2 (g) (‰) VPDB
δ13C C3 plants CO2
δ13C C4 plants CO2
δ13C Volcanic
δ13C Petroleum
δ13C soil CO2
δ13C atmospheric CO2
δ13C non-carbonate CO2
δ13C magmatic degassing CO2

Figure 11

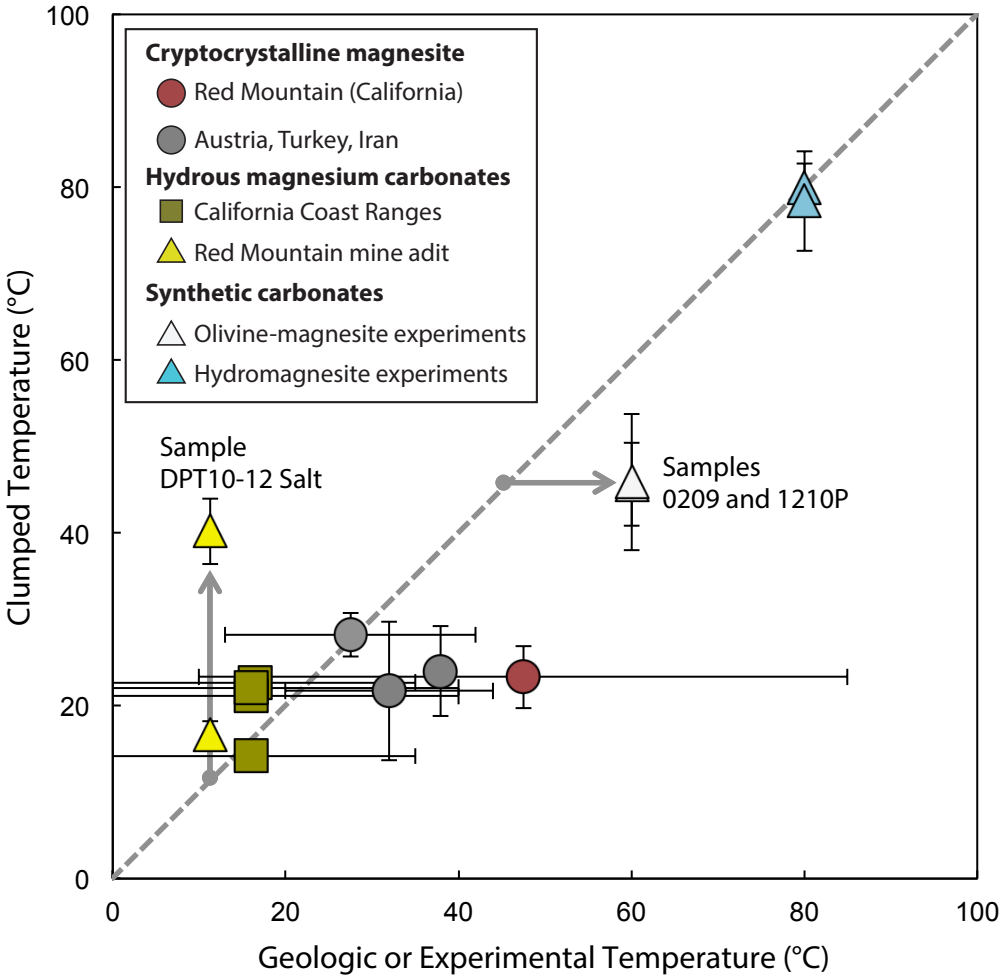
Cryptocrystalline magnesite
Red Mountain (California)
Austria, Turkey, Iran
Hydrous magnesium carbonates
California Coast Ranges
Red Mountain mine adit
Synthetic carbonates
Olivine-magnesite experiments
Hydromagnesite experiments
Sample
DPT10-12 Salt
Samples
0209 and 1210P
Clumped Temperature (°C)
Geologic or Experimental Temperature (°C)
0
20
40
60
80
100

Appendix A

Click here to download Appendix: 2016_Clumped_Appendix A Final.pptx

Appendix B

Click here to download Appendix: 2016_Clumped_Appendix B Final.docx

Electronic Annex

Click here to download Electronic Annex: 2016_Clumped_Appendix C.xlsx